A Theory of Synchrony by Coupling Through a Diffusive Chemical Signal

Jia Gou[1], Wei-Yin Chiang[4], Pik-Yin Lai[3], Michael J. Ward[1], and Yue-Xian Li[1,2]
[1]Dept. of Mathematics and [2]Dept. of Zoology,
Univ. of British Columbia, Vancouver, BC, Canada V6T 1Z2.
[3] Dept. of Physics, Graduate Institute of Biophysics, and Center for Complex Systems,
National Central Univ., Chungli, Taiwan 320, R.O.C.
[4] Dept. of Physics, Harvard University, 17 Oxford Street,
Cambridge, MA 02138, U.S.A.

February 2, 2016

Abstract

We formulate and analyze oscillatory dynamics associated with a model of dynamically active, but spatially segregated, compartments that are coupled through a chemical signal that diffuses in the bulk medium between the compartments. The coupling between each compartment and the bulk is due to both feedback terms to the compartmental dynamics and flux boundary conditions at the interface between the compartment and the bulk. Our coupled model consists of dynamically active compartments located at the two ends $x = 0$ and $x = 2L$ of a 1-D bulk region of spatial extent $2L$. The dynamics in the two compartments is modeled by Sel'kov kinetics, and the signalling molecule between the two-compartments is assumed to undergo both diffusion, with diffusivity D, and constant bulk degradation. For the resulting PDE-ODE system, we construct a symmetric steady-state solution and analyze the stability of this solution to either in-phase synchronous or anti-phase synchronous perturbations about the midline $x = L$. The conditions for the onset of oscillatory dynamics, as obtained from a linearization of the steady-state solution, are studied using a winding number approach. Global branches of either in-phase or anti-phase periodic solutions, and their associated stability properties, are determined numerically. For the case of a linear coupling between the compartments and the bulk, with coupling strength β, a phase diagram, in the parameter space D versus β is constructed that shows the existence of a rather wide parameter regime where stable in-phase synchronized oscillations can occur between the two compartments. By using a Floquet-based approach, this analysis with linear coupling is then extended to determine Hopf bifurcation thresholds for a periodic chain of evenly-spaced dynamically active units. Finally, we consider one particular case of a nonlinear coupling between two active compartments and the bulk. It is shown that stable in-phase and anti-phase synchronous oscillations also occur in certain parameter regimes, but as isolated solution branches that are disconnected from the steady-state solution branch.

1

Contact: Michael Ward, Department of Mathematics, UBC, Vancouver, BC, Canada V6T 1Z2. Tel: 604-822-5869. Email: ward@math.ubc.ca

1   Introduction

Individuals in a large network communicate with each other to engage and coordinate their activities. This happens at almost all levels of the living world ranging from a colony of unicellular amoebae to highly sophisticated social networks of people. In many cases, this communication is carried out through diffusive chemicals. Examples of such kind of systems range from the signalling of the amoebae *Dictyostelium discoideum* through the release of cAMP into the medium [5] where it diffuses and acts on each individual, to some endocrine neurons that secrete a hormone to the extracellular medium where it influences the secretion of this hormone from a pool of such neurons [15, 12], and to girls sharing a dormitory room leading to the synchronization of their menstrual cycles [16] presumably through the secretion of a pheromone [20, 22] in the shared space. Further examples where this kind of signalling occurs are related to quorum sensing behavior (cf. [3], [17], [18]). In many of these systems, the individual cells or localized units, can, under appropriate conditions, exhibit sustained temporal oscillations. In this way, signalling through a diffusive chemical often can switch on and/or off the oscillations and to synchronize the oscillations among all the individuals. The present paper is a theoretical investigation of the mechanism through which this kind of synchronization occurs.

Biological rhythms are ubiquitous in living organisms, especially in mammals including human being. Some of the best known examples are the circadian periodicity observed in the blood level of most hormones in mammals. Many hormones also exhibit rhythmicity with a period much shorter than the circadian rhythm. These rhythms are referred to as the ultradian rhythms. The rhythmicity in these hormones often plays a fundamental role in their physiological function. One of the best understood examples, and the one that we are motivated by, is the pulsatile variation in the concentration of gonadotropin-releasing hormone (GnRH) in the portal blood that circulates from the hypothalamus to the pituitary gland. This periodic signal of about one pulse per hour has been shown to be crucial in maintaining the normal reproductive activities in mammals [23]. It is now believed that 800-2000 GnRH neurons are scattered in a few areas of the hypothalamus. In order to generate a coherent pulsatile GnRH signal, such as is observed in the portal blood, synchronization of the secretory activities of the neurons is essential. In [14] a synchronization mechanism was proposed, whereby neurons are coupled through GnRH secreted into the extracellular space. Results from this model were shown to be consistent with *in vivo* experiments. The key limitation of this model of [14], however, was that it was assumed that extracellular space was continuously stirred so as to average out any spatial effects resulting from any chemical secretions. A more realistic model, would be to couple the diffusion of GnRH in the extracellular space to the localized secretory activity of individual neurons.

These past studies are the motivation for formulating and investigating a relatively new modeling

paradigm by which spatially segregated dynamically active units, such as cells or localized signalling compartments, communicate with each other through a signalling molecule that diffuses in the bulk medium between the active units. In our model that couples dynamically active compartments through a diffusive chemical signal, we will focus on the case where each compartment is a *conditional oscillator*. This term is adopted here to refer to a dynamical system that stays at a stable steady state when isolated from others, but is capable of generating sustained oscillations with some different choice of parameter values. Dynamics of the signal in extracellular space, referred to as the bulk region, is described by a simple diffusion equation, with diffusivity D, that undergoes linear bulk degradation. Each compartment is capable of sensing the strength of the signal, through either a linear or nonlinear coupling with the bulk, and responding to it by adjusting the rate of release of the signalling molecules into the bulk. The release of the signal by each compartment into the bulk region is modeled as a flux boundary condition at the interface between the compartment and the bulk.

In §2 we formulate such a 1-D model on the interval $0 < x < 2L$, which consists of a PDE-ODE system that couples diffusion in the bulk $0 < x < 2L$, with constant diffusivity D, to compartmental dynamics with Sel'kov kinetics on the boundaries $x = 0$ and $x = 2L$. The particular choice of Sel'kov kinetics, as originally used in [21] for modeling glycolysis oscillations, is not essential since the qualitative behavior of bulk-mediated oscillatory dynamics will also occur for other, more general, compartmental kinetics. In particular, for a related PDE-ODE membrane-bulk system the numerical study of [6] has revealed the possibility of stable synchronous dynamics under Fitzhugh-Nagumo reaction-kinetics in the compartments. However, in this model of [6], the coupling of the membrane to the bulk is different than for our Sel'kov model formulated in (2.1) below in that in [6] it was assumed that both the compartment and bulk concentrations are identical at the two membranes.

For our compartment-bulk model with Sel'kov kinetics, in §3 we consider the case where there is a linear coupling between the two compartments at $x = 0$ and $x = 2L$ and the bulk, where β represents the strength of this coupling. For this linearly coupled model, we construct a steady-state solution that is symmetric about the midline $x = L$. In §3.1 we then derive a transcendental equation for the eigenvalue parameter λ associated with the linearization of the coupled compartment-bulk model around the symmetric steady-state solution. In our stability theory, we must allow for perturbations that are either symmetric or anti-symmetric about the midline, which leads to the possibility of either in-phase synchronous or anti-phase synchronous instabilities in the two compartments. To determine unstable eigenvalues of the linearization, in Appendix A we use the winding number of complex analysis to determine the number of roots in $\text{Re}(\lambda) > 0$ to the transcendental equation for the eigenvalue. This linear stability analysis is supplemented by the numerical computation of global branches of periodic solutions, either in-phase or anti-phase, that bifurcate from the symmetric steady-state solution branch. These global solution branches, together with their stability properties, are determined using the numerical bifurcation software package XPPAUT [4] after first spatially discretizing the PDE-ODE system into a relatively large system of ODEs. In this way, a phase-diagram in the D versus β parameter space, characterizing the region where stable in-phase and anti-phase oscillations between the two compartments can occur is obtained. Our results show that there is a rather large parameter range where either stable in-phase or anti-phase oscillations occur. Full numerical computations of the PDE-ODE system of coupled compartmental-bulk dynamics, undertaken using a method-of-lines approach, are used to validate the theory.

In §4, we extend the simple two-compartment case of §3 to allow for a periodic chain of evenly-spaced dynamically active units that are linearly coupled to a bulk diffusion field. By using an approach based

on Floquet theory, we analyze the linear stability problem to determine Hopf bifurcation thresholds associated with the various possible modes of oscillation. Comparisons of predictions from the linear stability theory with full numerical simulations are performed.

In §5 we illustrate oscillatory compartmental dynamics for a specific type of nonlinear coupling between the bulk and the two compartments, for which the steady-state solution is the same as that for the uncoupled compartmental dynamics. For this model, no Hopf bifurcations can occur along the steady-state solution branch. Nevertheless, we show using the numerical bifurcation software XPPAUT [4] that this model can still generate compartment-bulk oscillations. More specifically, our numerical computations show, in contrast to the case of a linear coupling between the compartments and the bulk considered in §3, that the branches of in-phase and anti-phase periodic solutions are disconnected and do not bifurcate off of the symmetric steady-state solution branch. Our global bifurcation diagram reveals that there is a parameter range of bistability where either stable in-phase oscillations or stable anti-phase oscillations can co-exist with the stable symmetric steady-state solution branch. Although the coupled system in §5 is only a mathematical model, and is not motivated by a specific biological context, the analysis does indicate that the coupling of active compartments by bulk diffusion can lead to disconnected global branches of periodic solutions having a saddle-node structure. This indicates that hysteretic behavior in the compartment-bulk oscillations can be possible as parameters are varied. In §5.1 we study an extended ODE compartmental dynamics model, closely related to the nonlinear coupled compartment-bulk model, but where bulk diffusion is neglected. Finally, in §6 we outline a few potential extensions of the theory to more biologically realistic systems.

Related recent investigations of oscillatory dynamics due to membrane-bulk coupling are that of [7], [8], and [9]. In [7], a center manifold analysis was used to analyze the parameter space near a double Hopf point, corresponding to the intersection of the Hopf boundaries for the in-phase and anti-phase modes. This co-dimension-2 double Hopf point leads to the existence of an invariant torus in the dynamics. In [8] a detailed linear stability theory was given for a general class of coupled membrane-bulk models with only one active component on the membrane. For this class, a weakly nonlinear analysis, leading to an amplitude equation, was derived to distinguish whether Hopf bifurcations from the steady-state are subcritical or supercritical. Finally, in [9] oscillatory instabilities were analyzed for the coupled membrane-bulk model of [6], which has slow-fast Fitzhugh-Nagumo compartment reaction-kinetics. As a result of the analytical simplification resulting from the assumed slow-fast membrane kinetics, in [9] it was largely possible to analyze the linear stability problem using asymptotic methods.

The present study differs from the [8] in that we focus on the case where there are, not one, but instead two active components in each compartment, and where the reaction-kinetics have no slow-fast dynamics, as was assumed in [9]. As such, we develop and illustrate a hybrid analytical-numerical approach to analyze the linear stability problem and to compute global branches of periodic solutions. We also examine oscillatory instabilities for the novel setting of a periodic chain of dynamically active components, which has not been considered previously. Finally, we illustrate through a particular nonlinearly coupled "toy" model, that periodic solution branches induced by membrane-bulk coupling can exhibit saddle-node behavior, and do not necessarily arise from Hopf bifurcations of the steady-state problem.

4

2 Formulation of the Coupled Compartment-Bulk Model

We begin by formulating a simple model that describes the diffusion and degradation of a signalling particle in a 1-D spatial domain. The concentration/density of the particle is represented by $C(x, t)$, defined on the bulk $x \in [0, 2L]$ at time t. Two identical compartments are introduced at the two ends of the interval. These compartments can either be regarded as two cells or two dynamically active membranes, which can interact with the diffusive signalling particle in the bulk. The dynamical process in each compartment, be it biochemical reactions inside a cell or other chemical reactions on the membrane, is described by a system of nonlinear ODEs. However, the dynamical process in each compartment is modulated by the concentration of the diffusive particle near each boundary. Thus, the dynamics in the compartment at the left end depends on $C(0, t)$, while the one at the right end is modulated by $C(2L, t)$. The release of signalling particles from the compartments into the bulk is modeled as a flux boundary condition at each of the two compartments. In the bulk, we model the diffusion process as

$$\frac{\partial C}{\partial t} = DC_{xx} - kC, \qquad 0 < x < 2L, \quad t > 0,$$
$$-DC_x(0, t) = \kappa(V_0(t) - C(0, t)), \qquad DC_x(2L, t) = \kappa(V_1(t) - C(2L, t)). \tag{2.1a}$$

Here $D > 0$ and $k > 0$ are the constant diffusion and bulk degradation rates, respectively, $\kappa > 0$ measures the strength (in unit of length per time) of chemical flux secreted by the cells, while $V_i(t)$ ($i = 0, 1$) are the concentrations of the particle in the two compartments. In our model, we assume the efflux of particles out of each compartment is proportional to the difference between the concentration inside each compartment and that outside of it in the bulk. Therefore, the influence of each compartment on the diffusive particles is described by the linear flux boundary condition of (2.1a).

The dynamics governing the time evolution of the concentration $V_i(t)$ and another variable $W_i(t)$ inside each compartment is described by the following system of nonlinear ODEs:

$$\frac{dV_i}{dt} = f(V_i, W_i) + \beta P(C(2Li, t), V_i(t)), \qquad \frac{dW_i}{dt} = g(V_i, W_i); \qquad \text{for} \quad i = 0, 1. \tag{2.1b}$$

For simplicity, we assume that the compartment kinetics $f(V, W)$ and $g(V, W)$, as well as the coupling term $\beta P(C(2Li, t), V(t))$ to the bulk, are identical for the two compartments. We assume that this system, when isolated (i.e. when $\beta = 0$), and given favourable choices of parameter values, is capable of generating sustained oscillations of limit cycle type. In addition, we further assume that, when isolated, the compartmental dynamics has a unique stable steady-state.

To illustrate the new behavior that can be induced by compartment-bulk coupling, we will use Sel'kov model, for which the kinetics are

$$f(V, W) = \alpha W + WV^2 - V, \qquad g(V, W) = \epsilon \left[\mu - (\alpha W + WV^2) \right], \tag{2.1c}$$

where $0 < \epsilon < 1$ is a parameter. We remark that the qualitative conclusions derived in the present study do not depend on the specific forms of the reaction kinetics, provided that limit cycle type oscillations in the dynamics can occur. In our model, the influence of the concentration of particles near each boundary on the compartment dynamics is described by the coupling term $\beta P(C(2Li, t), V)$, where β represents the coupling strength. Two types of coupling will be considered. In §3 we consider a linear coupling

term, while in §5 we consider a specific form of nonlinear coupling. In §4 we generalize (2.1) to consider a periodic chain of evenly-spaced compartments with linear coupling.

For this Sel'kov model, when each compartment is isolated, i.e. when $\beta = 0$, there is a unique steady state solution given by $V_{e0} = \mu$ and $W_{e0} = \mu/(\alpha + \mu^2)$, which is stable. In other words, the two compartments are "conditional oscillators" when decoupled from each other. Therefore, when oscillations occur in the present study, they are caused by the coupling between the two compartments induced by the diffusive signalling particles.

3 Linear Coupling Between the Compartments and the Bulk

We first consider (2.1) with a linear coupling term $P(C(2Li, t), V)$ where $i = 0, 1$. We specify that

$$P(C(2Li, t), V) = C(2Li, t) - V(t), \qquad i = 0, 1. \tag{3.1}$$

With this choice, all interactions between the compartments and the diffusive particles are linear.

We first determine a steady-state solution to (2.1), with (3.1), that is symmetric about the midline $x = L$. To construct this steady-state solution we solve (2.1) on $0 < x < L$, while imposing a no-flux boundary condition for C at $x = L$. Since only the compartment at the left boundary $x = 0$ is considered, we drop the subscripts for the compartmental variables V and W. We readily calculate that there is a unique symmetric steady-state solution $C_e(x)$, V_e, and W_e, given by

$$C_e(x) = C_e^0 \frac{\cosh(\omega(L - x))}{\cosh(\omega L)}, \qquad C_e^0 = \frac{\kappa \mu}{\kappa + D\omega \tanh(\omega L)(1 + \beta)}, \qquad \omega \equiv \sqrt{k/D},$$

$$V_e = \frac{\mu}{1 + \beta} + \frac{\beta C_e^0}{1 + \beta}, \qquad W_e = \frac{\mu}{\alpha + V_e^2}. \tag{3.2}$$

The steady-state solution in the compartment for the coupled system differs from that of the uncoupled problem, and reduces to $V_e = V_{e0} \equiv \mu$ and $W_e = W_{e0} \equiv \mu/(\alpha + \mu^2)$ in the absence of coupling.

3.1 Linear Stability Analysis of the Steady State

To analyze the linear stability of the symmetric steady-state solution, we introduce the perturbation

$$C(x, t) = C_e(x) + e^{\lambda t}\eta(x), \qquad V(t) = V_e + e^{\lambda t}\varphi, \qquad W(t) = W_e + e^{\lambda t}\phi, \tag{3.3}$$

into (2.1). Upon linearizing the resulting system, we obtain the following eigenvalue problem for λ:

$$\lambda\eta = D\eta_{xx} - k\eta, \qquad 0 < x < L; \qquad -D\eta_x(0) = \kappa(\varphi - \eta_0), \tag{3.4a}$$

$$\lambda\varphi = f_V^e \varphi + f_W^e \phi + \beta\left(P_C^e \eta_0 + P_V^e \varphi\right), \qquad \lambda\phi = g_V^e \varphi + g_W^e \phi. \tag{3.4b}$$

Here we have defined $\eta_0 \equiv \eta(0)$, $f_V^e \equiv f_V(V_e, W_e)$, $f_W^e \equiv f_W(V_e, W_e)$, $P_C^e \equiv P_C(C_e^0, V_e)$, etc.

The formulation of the linear stability problem is complete after imposing a boundary condition for $\eta(x)$ on the midline $x = L$. We will consider two distinct choices. The choice $\eta(L) = 0$ corresponds to an anti-phase synchronous perturbation, while the condition $\eta_x(L) = 0$ corresponds to an in-phase synchronization of the two compartments. We will consider both possibilities in our analysis below.

For either choice of the boundary condition, we can readily solve (3.4) to derive that λ must be a root of the transcendental equation $\mathcal{F}(\lambda) = 0$, where $\mathcal{F}(\lambda)$ is defined by

$$\mathcal{F}(\lambda) \equiv \frac{1}{p_\pm(\lambda)} - \frac{g_W^e - \lambda}{\det(J_e - \lambda I)}, \qquad J_e \equiv \begin{pmatrix} f_V^e, & f_W^e \\ g_V^e & g_W^e \end{pmatrix}. \tag{3.5a}$$

Here J_e is the Jacobian matrix of the uncoupled compartmental dynamics evaluated at the steady-state (3.2) for the coupled system. In (3.5a), $p_\pm(\lambda)$ are defined by

$$p_+(\lambda) \equiv \frac{\beta D \Omega_\lambda \tanh(\Omega_\lambda L)}{\kappa + D \Omega_\lambda \tanh(\Omega_\lambda L)}, \qquad p_-(\lambda) \equiv \frac{\beta D \Omega_\lambda \coth(\Omega_\lambda L)}{\kappa + D \Omega_\lambda \coth(\Omega_\lambda L)}, \qquad \Omega_\lambda \equiv \sqrt{\frac{k + \lambda}{D}}, \tag{3.5b}$$

where p_+ corresponds to in-phase synchronous perturbations, while p_- corresponds to anti-phase synchronous perturbations. In (3.5b), we must specify the principal branch of the square root to ensure that $\eta(x)$ is analytic in $\mathrm{Re}(\lambda) > 0$.

To classify any instabilities that can occur with compartment-bulk coupling we need to determine the number of roots of (3.5a) and their distribution in the right-half of the complex λ-plane (i.e. $\mathrm{Re}(\lambda) > 0$). We will approach this problem in two ways. One method is to numerically implement a winding number approach, as done below in Appendix A. The second method, which we discuss here, is to use the bifurcation software XPPAUT[4]. Firstly, we spatially discretize (2.1) into a relatively large system of ODEs, and then we use XPPAUT to path-follow solution branches that bifurcate off the steady-state solution (3.2). In this way, in Fig. 2 we show two typical bifurcation diagrams with respect to the diffusivity D and the coupling strength β, for fixed values of the other parameters as shown in the figure caption. As seen from these plots, there are Hopf bifurcation points at which the steady-state solution loses its stability to either in-phase or anti-phase oscillatory instabilities in the two compartments. Moreover, in some regions of the (β, D) parameter space only either the in-phase or anti-phase mode is present. In the left panel of Fig. 2, where we plot the bifurcation diagram for V versus D when $\beta = 0.8$, we observe that the in-phase and anti-phase periodic solution branches change stability at $D \approx 0.25$ and $D \approx 0.55$, respectively, which correspond to Torus bifurcation points. By tuning the parameter β, these bifurcation points can occur at a common value of D, and correspond to the intersection of the black and magenta curves in Fig. 1. For this co-dimension-2 case, such Torus bifurcations, leading to the existence of an invariant Torus in the dynamics, were analyzed in detail using a center manifold approach in [7]. For $\beta = 0.8$, we further observe from the left panel of Fig. 2 that both the in-phase and anti-phase oscillations are stable on the range $0.25 < D < 0.55$. A similar bifurcation diagram, but with fixed $D = 0.4$ and β a parameter, is shown in the right panel of Fig. 2.

By varying the values of D and β, we can obtain a series of bifurcation diagrams, representing slices through the (β, D) phase space. By amalgamating these slices, we generate the phase diagram in the (β, D) parameter plane as shown in Fig. 1. We remark that the diffusivity D effectively represents the length scale of this system. When D is small, effectively the distance between the two cells is large. However, when D is large, effectively one can consider that the two cells are close together. Therefore, changing D is equivalent to changing the distance between the two cells. Variations in the coupling strength β determine the importance of the feedback in the compartment-bulk interactions.

The phase diagram in Fig. 1 shows the region of stability of the steady-state solution, and regions where either in-phase or anti-phase oscillations, or both, can occur as the diffusivity D and the coupling strength β are varied. From this plot, we observe that when D is relatively small, then as the coupling
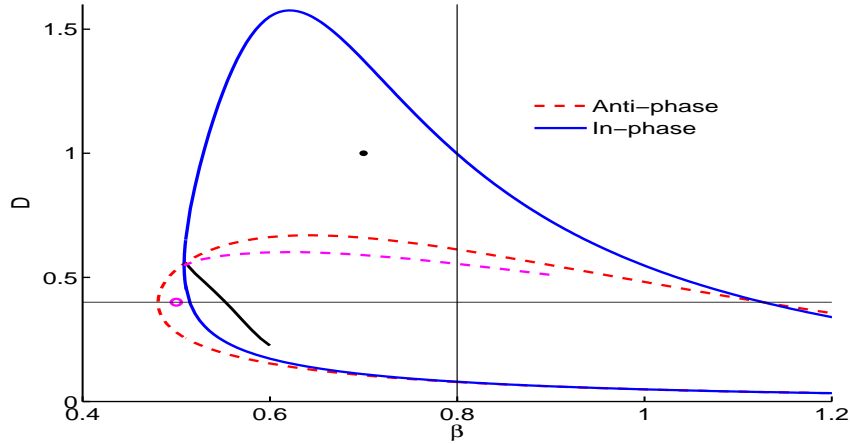
Figure 1: Phase diagram in the D versus β parameter plane, for the Sel'kov model (2.1) with linear coupling (3.1) for both the in-phase and anti-phase modes. The parameters in (2.1) are $\mu = 2$, $\alpha = 0.9$, $\epsilon = 0.15$, and $\kappa = k = L = 1$. In-phase and anti-phase compartmental oscillations occur within loop bounded by the blue solid and red-dashed curves, respectively. Above the black solid line, the in-phase periodic solution is stable, while below the dashed magenta curve the anti-phase periodic solution is stable. The horizontal and vertical slices at $D = 0.4$ and $\beta = 0.8$, respectively, through the phase diagram are discussed in Fig. 2.
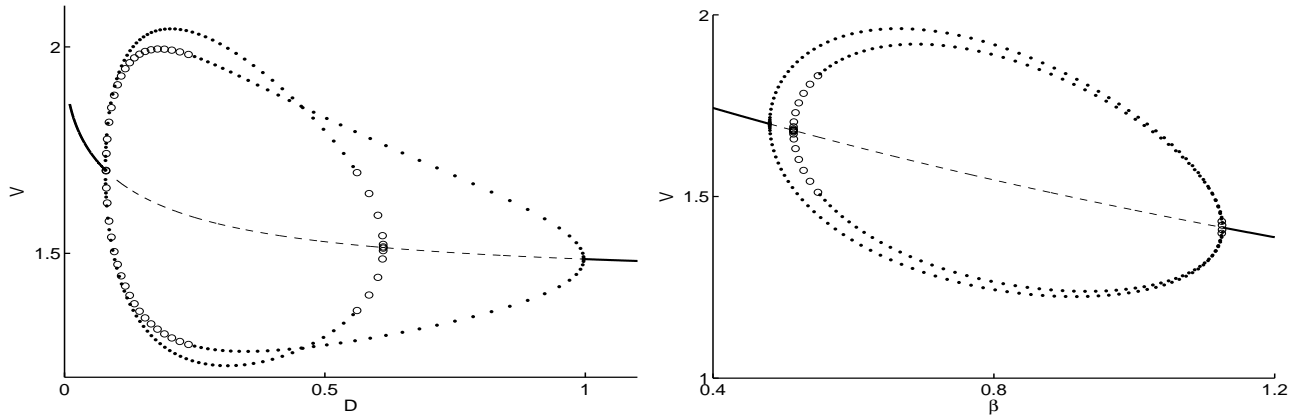

Figure 2: Bifurcation diagram of V corresponding to the vertical and horizontal slices through the phase diagram of Fig. 1, as computed using XPPAUT [4]. Left panel: V versus D for $\beta = 0.8$ (vertical slice). Right panel: V versus β for $D = 0.4$ (horizontal slice). The solid and dashed lines denote linearly stable and unstable branches of steady-state solutions, respectively. The two closed loops correspond to branches of in-phase and anti-phase periodic solutions. In the left panel, the branch that bifurcates from the steady-state near $D = 1$ is the in-phase synchronous branch and in the right panel, the outer loop is the anti-phase branch. The solid/open circles on these loops denote linearly stable/unstable periodic solutions, respectively.

strength β is increased it is the anti-phase mode that becomes unstable first. This phenomenon is also plausible biologically, since when D and β are both small the communication between the two cells is not very efficient, and so it is difficult to synchronize their dynamics with a common phase.
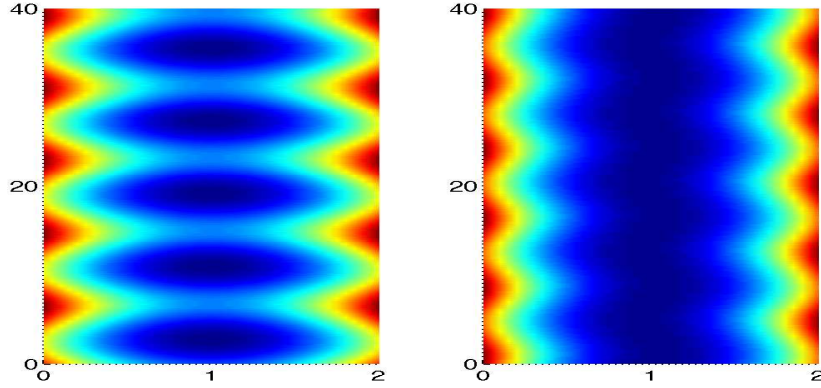

Figure 3: Full numerical solutions of the PDE-ODE system (2.1) demonstrating either in-phase or anti-phase oscillations of the two compartments. Time increases from bottom to top and the horizontal axis indicate the bulk region where $L = 1$. Left panel: in-phase oscillations for $D = 1$ and $\beta = 0.7$ (black dot in Fig 1). Right panel: anti-phase oscillations for $D = 0.4$ and $\beta = 0.5$ (magenta open circle in Fig. 1.) The other parameter values are the same as in the caption of Fig.1.

From Fig. 1, we also observe that when D is relatively large, only the in-phase synchronized oscillation can occur. In the region of Fig. 1 bounded by the blue solid curve, the steady-state solution is unstable to the in-phase mode, but it is only above the black solid curve where a stable in-phase synchronized oscillation between the two compartments can occur. Similarly, inside the red dashed curve, the steady-state solution is unstable to the anti-phase mode, but it is only under the magenta dashed curve where the anti-phase mode is stable. Therefore, in the region of Fig. 1 bounded by the black and magenta curves, stable in-phase and stable anti-phase periodic oscillations can co-exist. The determination of which mode would result from numerical computations of the initial value problem (2.1) should depend on the initial conditions at time $t = 0$.

To confirm predictions obtained from the bifurcation analysis, full time-dependent numerical solutions of the coupled PDE-ODE system (2.1) were computed using a method of lines approach based on a second-order spatial discretization of the bulk diffusion operator. In our computation, we picked two points in the phase diagram in Fig. 1 indicated in the figure by the black solid dot and the magenta open circle. For these parameter sets, full numerical solutions of the PDE-ODE system (2.1) are shown in Fig. 3 starting with the initial value $C(x, 0) = 0.2$, and with randomly generated initial values for V_i and W_i for $i = 0, 1$ at $t = 0$. The plots in Fig. 3 for t large confirm the theoretical predictions of the phase diagram by showing in-phase synchronous oscillations for $D = 1$ and $\beta = 0.7$ (left panel), and anti-phase synchronous oscillations for $D = 0.4$ and $\beta = 0.5$ (right panel).

Finally, we remark that if we fix a point in the phase diagram where both the in-phase and anti-phase modes are stable, it is possible to evolve to either of these two modes depending on the initial condition. For instance, if we take $\beta = 0.8$ and $D = 0.4$, then both modes of oscillation are stable, as seen from Fig. 2. For the initial values $C(x, 0) = 0.5$ with $v_1 = 0.3$, $w_1 = 0.2$, $v_2 = 0.4$, and $w_2 = 0.2$ at $t = 0$,

9

our numerical simulation of the PDE-ODE system (2.1) in Fig. 4 shows in-phase oscillations after some transient period. For the same initial values, but changing v_1 and w_1 to $v_1 = 5$ and $w_1 = 10$, we obtain anti-phase oscillations.
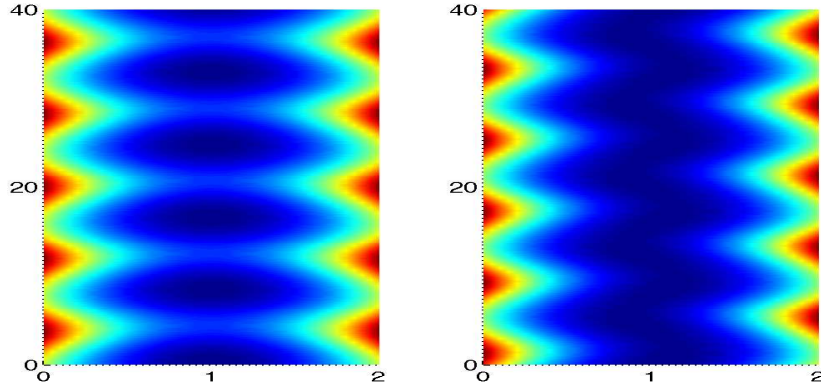
3.2 The Winding Number Computation

Figure 4: Full numerical solutions of the PDE-ODE system (2.1) for $D = 0.4$ and $\beta = 0.8$, showing different long-time results depending on the initial conditions. Left panel: for the initial values $C(x,0) = 0.5$, $v_1 = 0.3$, $w_1 = 0.2$, $v_2 = 0.4$, and $w_2 = 0.2$, there are in-phase oscillations. Right panel: with the same initial values, but with $v_1 = 5$ and $w_1 = 10$, we get anti-phase oscillations.

In Appendix A, we use the winding number criterion of complex analysis to determine the number of roots of $\mathcal{F}(\lambda) = 0$ in $\text{Re}(\lambda) > 0$, where $\mathcal{F}(\lambda)$ is defined in (3.5). The analysis is similar to that used in [19] to analyze the stability of localized pulse solutions to reaction-diffusion systems.

Let Γ_{I_+} denote the positive imaginary axis $\lambda = i\lambda_I$ with $\lambda_I > 0$ traversed in the downwards direction. Then, as shown in Appendix A, the change in the argument of $\mathcal{F}(\lambda)$ on Γ_{I_+}, denoted by $\left[\arg \mathcal{F}\right]\big|_{\Gamma_{I_+}}$, can only be an integer number of 2π, so that $\left[\arg \mathcal{F}\right]\big|_{\Gamma_{I_+}} = 2m\pi$ for $m = 0, \pm 1, \pm 2, \ldots$. As derived in Appendix A, the number N of zeroes of $\mathcal{F}(\lambda) = 0$ in $\text{Re}(\lambda) > 0$ is

$$N = 2m + P, \qquad P = \begin{cases} 2, & \text{when} \quad \text{tr}(J_e) > 0, \\ 0, & \text{when} \quad \text{tr}(J_e) < 0. \end{cases} \tag{3.6}$$

Although we cannot, in general, determine m analytically, it is readily calculated numerically from (3.5a). To illustrate the numerical computation of the winding number, we consider (2.1) with the linear coupling (3.1) for the parameter value $D = 1$ and $\beta = 0.7$, corresponding to the marked black dot in Fig. 1. The other parameter values for (2.1) are given in the caption of Fig. 1. For this parameter set we calculate that $\text{tr}(J_e) > 0$ so that $P = 2$ from (3.6). In the right panel of Fig. 5, we plot the path of $\mathcal{F}(i\lambda_I)$ in the $(\mathcal{F}_R, \mathcal{F}_I)$ parameter plane for both the in-phase synchronous mode (solid curve) and the anti-phase synchronous mode (dashed curve). For the anti-phase mode we observe that as λ_I decreases from a very

large initial value, $\mathcal{F}(\lambda)$ wraps around the origin once in clockwise direction, so that $[\arg \mathcal{F}]|_{\Gamma_{I_+}} = -2\pi$. Therefore, since $m = -1$, we get $N = 0$ from (3.6). In contrast, for the in-phase synchronous mode we observe from Fig. 5 that $[\arg \mathcal{F}]|_{\Gamma_{I_+}} = 0$, so that $m = 0$ and $N = 2$ from (3.6). These winding number computations show that, at this parameter set, the steady-state solution is unstable only to in-phase synchronous perturbations.
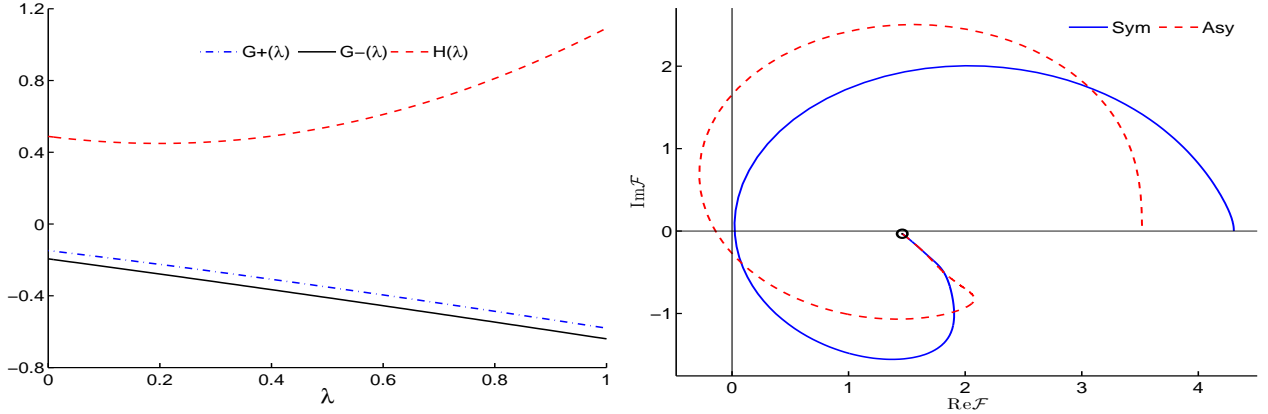

Figure 5: Left panel: $G_+(\lambda)$, $G_-(\lambda)$, and $H(\lambda)$, as defined in (3.7), are plotted on $\lambda > 0$ real for $D = 1$ and $\beta = 0.7$, with the other parameters as in the caption of Fig. 1. There is no intersection $G_\pm(\lambda)$ and $H(\lambda)$, which shows that $\mathcal{F}(\lambda)$ has no real roots λ for either the in-phase and anti-phase modes. Right panel: $\mathcal{F}_I(\lambda_I) = \mathrm{Im}(\mathcal{F}(i\lambda_I))$ is plotted versus $\mathcal{F}_R(\lambda_I) = \mathrm{Re}(\mathcal{F}(i\lambda_I))$ for both the in-phase and anti-phase modes as λ_I is decreased from 1000 to 0. The open circle represents the starting point at $\lambda_I = 1000$. For the anti-phase mode (dashed curve), we have $m = -1$ in (3.6) since the trajectory wraps around the origin once in the clockwise direction. For the in-phase mode (solid curve), the plot shows that $m = 0$ in (3.6).

To determine the location of the two unstable eigenvalues for the in-phase synchronous mode when $D = 1$ and $\beta = 0.7$ we seek roots of $\mathcal{F}(\lambda)$ on the positive real axis $\lambda > 0$. To do so, we conveniently rewrite $\mathcal{F}$ as

$$\mathcal{F}(\lambda) = \frac{H(\lambda) - G_\pm(\lambda)}{p_\pm(\lambda)\det(J_e - \lambda I)}, \qquad \text{where} \quad H(\lambda) \equiv \det(J_e - \lambda I), \qquad G_\pm(\lambda) \equiv p_\pm(\lambda)(g_W^e - \lambda). \tag{3.7}$$

In the left panel of Fig. 5 we plot $H(\lambda)$ and $G_\pm(\lambda)$ on $\lambda > 0$ real for $D = 1$ and $\beta = 0.7$. This plot shows that there are no intersections between $H(\lambda)$ and $G_\pm(\lambda)$. Since, consequently, there is no real positive root to $\mathcal{F}(\lambda) = 0$, we conclude that the initial instability associated with the in-phase-mode is an in-phase synchronous oscillatory instability of the compartmental dynamics. A bifurcation diagram (not shown) similar to that in Fig. 2 predicts that this initial instability leads to a large-scale stable in-phase synchronous oscillation. The full numerical results of the PDE-ODE system (2.1) shown in the left panel of Fig. 3, as computed using a method of lines approach, confirms this prediction of a stable synchronous oscillation.

We remark that this strategy of computing the winding number, and then using (3.6) to determine N, was used for mapping out the regions in the phase diagram of Fig. 1 characterizing the linear stability properties of the steady-state solution to either in-phase or anti-phase perturbations.

11

4 A Periodic Chain of Active Units Coupled by Bulk Diffusion

In this section we extend the analysis in §3 to the case where m identical compartments, or cells, are evenly-spaced, with spacing $2L$, on a 1-D ring. These cells are then coupled by a bulk-diffusion field. A schematic diagram of this periodic arrangement of active cells is shown in the left panel of Fig. 6. Equivalently, we consider a 1-D domain on the interval $[-L, (2m-1)L]$, with cells located at $2jL$ for $j = 0, \ldots, m-1$, with the imposition of periodic boundary conditions for the bulk diffusion field at the endpoints. A schematic plot of four such cells is shown in the right panel of Fig. 6.
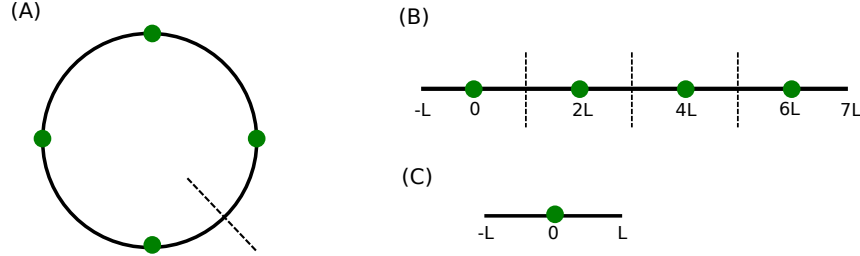

Figure 6: Left panel: Schematic diagram of four identical cells on a ring structure. The green solid dots represent cells. Top right panel: Schematic diagram of four identical cells on the domain $[-L, 7L]$ with periodic boundary conditions at the two ends. Bottom right panel: schematic of one cell on $[-L, L]$.

With the same notation used in §2, we model the system with m identical cells on a 1-D structure as follows. Firstly, the bulk diffusion process is modeled by

$$C_t = DC_{xx} - kC, \quad t > 0, \quad x \in (-L, (2m-1)L), \quad \text{with} \quad x \neq 2jL, \quad j = 0, \ldots, m-1,$$
$$C(-L, t) = C(2mL - L, t), \quad C_x(-L, t) = C_x(2mL - L, t). \tag{4.1a}$$

Inside each cell, we suppose that there are n locally interacting chemicals species. As shown in Appendix B, the local dynamics in each cell, with the linear coupling to the bulk diffusion field, is governed by

$$\frac{d\boldsymbol{u_j}}{dt} = \boldsymbol{F}(\boldsymbol{u_j}) + \boldsymbol{e_1} \left[\frac{\kappa}{2} \left(C(2jL^+, t) + C(2jL^-, t) \right) - \kappa u_{1j} \right], \qquad j = 0, \ldots, m-1, \tag{4.1b}$$

where $\boldsymbol{u_j} = (u_{1j}, u_{2j}, \ldots, u_{nj})^T$ denotes the n species inside the j-th cell, $\boldsymbol{e_1} \equiv (1, 0, \ldots, 0)^T$, with u_{1j} being the first chemical species inside the jth cell. Moreover, $\boldsymbol{F}$ is the common local reaction kinetics, since the cells are assumed to be identical. Here $C(2jL^-, t)$ and $C(2jL^+, t)$ represent the bulk concentration field at the left and right boundary of the j-th cell. As shown in Appendix B, the boundary conditions for the bulk concentration C at the cell boundaries, where $j = 0, \ldots, m-1$, are

$$DC_x(2jL^+, t) = \kappa \left(C(2jL^+, t) - u_{1j}(t) \right), \quad DC_x(2jL^-, t) = \kappa \left(u_{1j}(t) - C(2jL^-, t) \right), \tag{4.1c}$$

where $\kappa > 0$ is the common cell permeability parameter.

We remark that in our formulation, we have only assumed that $C(x, t)$ is piecewise continuous on the ring, and so in general $C(2jL^+, t) \neq C(2jL^-, t)$. An alternative, but simpler formulation, would be to impose that C is continuous on the ring, and that there is a jump in the flux DC_x across each cell. Although we do not pursue this simpler problem here, the linear stability analysis associated with this problem is discussed briefly in Appendix C.

4.1 The Steady-State Solution

We first calculate the symmetric steady-state solution of (4.1). For this steady-state, the bulk concentration is symmetric with respect to the midline of every two cells, and the local cell variables are the same for each cell. Although there might be other asymmetric steady-state solutions for the full system (4.1) of m coupled cells, we focus only on the symmetric steady-state solution and its linear stability properties.

To construct the symmetric steady-state, we need only consider the domain $[-L, L]$, as shown in Fig. 6, with a cell located at $x = 0$ and with periodic boundary conditions at $x = \pm L$. We denote this steady-state solution by $C^e(x)$ and the corresponding local steady-state cell variables as $\boldsymbol{u}^e$. Then the symmetric steady-state solution for C in the full system (4.1) is constructed by a simple period extension of this basic solution. Hence, focusing on the interval $[-L, L]$, the steady-state solution $C^e(x)$ satisfies

$$
C^e_{xx} = \frac{k}{D} C^e, \quad x \in (-L, 0) \cup (0, L); \qquad C^e(-L) = C^e(L), \quad C^e_x(-L) = C^e_x(L),
$$
$$
DC^e_x(0^+) = \kappa \left(C^e(0^+) - u^e_1 \right), \quad DC^e_x(0^-) = \kappa \left(u^e_1 - C^e(0^-) \right).
$$
(4.2)

The steady-state solution for the compartmental variable $\boldsymbol{u}^e$ satisfies

$$
\boldsymbol{F}(\boldsymbol{u^e}) + \boldsymbol{e_1} \left[\frac{\kappa}{2} \left(C^e(0^+) + C^e(0^-) \right) - \kappa u^e_1 \right] = 0.
$$
(4.3)

On each subinterval, we can calculate the steady state solution $C^e(x)$ separately as

$$
C^e(x) = \begin{cases} A \cosh((x - L)\omega), & 0 < x < L, \\ A \cosh((x + L)\omega), & -L < x < 0, \end{cases}
$$
(4.4a)

where A and ω are given by

$$
\omega \equiv \sqrt{\frac{k}{D}}, \qquad A = \frac{\kappa u^e_1}{\kappa \cosh(L\omega) + D\omega \sinh(L\omega)}.
$$
(4.4b)

As expected this steady-state is continuous across the cells.

For the special case where the local cell variable $\boldsymbol{u}$ has two components $\boldsymbol{u} = (V, W)^T$ with local reaction term $\boldsymbol{F} = (f, g)^T$, where f and g are the Sel'kov kinetics given in (2.1c), we can use (4.3) and (4.4) to explicitly identify a unique steady-state V^e and W^e as

$$
V^e = \frac{\mu(\kappa + D\omega \tanh(L\omega))}{\kappa + (1 + \kappa)D\omega \tanh(L\omega)}, \qquad W^e = \frac{\mu}{\alpha + (V^e)^2}.
$$
(4.4c)

4.2 The Linear Stability Analysis

Next, we study the linear stability of the steady-state solution (4.4) for the case of Sel'kov kinetics. By introducing the perturbation (3.3) into (4.1) and linearizing, we obtain the eigenvalue problem

$$
\eta'' = \frac{(k + \lambda)}{D} \eta, \qquad x \in (-L, (2m - 1)L), \quad \text{with} \quad x \neq 2jL, \quad j = 0, \ldots, m - 1,
$$
$$
D\eta'(2jL^+) = \kappa(\eta(2jL^+) - \varphi), \quad D\eta'(2jL^-) = \kappa(\varphi - \eta(2jL^-)), \quad j = 0, \ldots, m - 1,
$$
(4.5a)

13

subject to the periodic boundary conditions

$$\eta(-L) = \eta(2mL - L), \qquad \eta'(-L) = \eta'(2mL - L). \tag{4.5b}$$

Upon linearizing the reaction kinetics we have that

$$\lambda\varphi = f_V^e\varphi + f_W^e\phi - \kappa\varphi + \frac{\kappa}{2}\left(\eta(0^+) + \eta(0^-)\right), \qquad \lambda\phi = g_V^e\varphi + g_W^e\phi, \tag{4.5c}$$

where f_V^e, f_W^e, g_V^e, and g_W^e are evaluated at the steady-state (4.4c).

Instead of considering (4.5a) with periodic boundary condition (4.5b), we make use of Floquet theory and consider (4.5a) on the fundamental interval $[-L, L]$ with the Floquet boundary conditions

$$\eta(L) = z\eta(-L), \quad \eta'(L) = z\eta'(-L). \tag{4.6}$$

The solution can then be extended to the interval $[L, 3L]$ by defining $\eta(x) \equiv z\eta(x - 2L)$ for $x \in [L, 3L]$ and using translation invariance. Since the m cells are identical, it is clear that $\eta(x)$ satisfies (4.5a). By iterating this process, we construct the solution of (4.5a) on the whole domain $[-L, (2m - 1)L]$ provided that $\eta(2mL - L) = z^m\eta(-L)$. Therefore, we obtain that z must be one of the m-th roots of unity

$$z \equiv e^{2\pi i l/m}, \quad \text{where} \quad l = 0, \ldots, m - 1. \tag{4.7}$$

In this way we have recovered the periodic solution to (4.5a) on $[-L, (2m - 1)L]$.

Next, we solve (4.5a) on $[-L, L]$ subject to the Floquet boundary conditions (4.6). The solution to (4.5a) and (4.6) is

$$\eta(x) = \begin{cases} [zA\cosh((x - L)\Omega_\lambda) + zB\sinh((x - L)\Omega_\lambda)]\,\varphi, & 0 < x < L, \\ [A\cosh((x + L)\Omega_\lambda) + B\sinh((x + L)\Omega_\lambda)]\,\varphi, & -L < x < 0, \end{cases} \tag{4.8}$$

where A, B, and Ω_λ are defined by

$$A \equiv \frac{\kappa(z + 1)/z}{2D\Omega_\lambda\sinh(L\Omega_\lambda) + 2\kappa\cosh(L\Omega_\lambda)}, \quad B \equiv \frac{\kappa(z - 1)/z}{2D\Omega_\lambda\cosh(L\Omega_\lambda) + 2\kappa\sinh(L\Omega_\lambda)}, \quad \Omega_\lambda \equiv \sqrt{\frac{k + \lambda}{D}}, \tag{4.9}$$

and where we choose the principal branch of Ω_λ if λ is complex. From this solution we then calculate

$$\eta(0^+) + \eta(0^-) = A(z + 1)\cosh(\Omega_\lambda L) + B(1 - z)\sinh(\Omega_\lambda L). \tag{4.10}$$

Upon substituting these expressions into (4.5c), we obtain a homogeneous linear system for φ and ϕ given by

$$(f_V^e + \Delta_\lambda)\varphi + f_W^e\phi = \lambda\varphi, \qquad g_V^e\varphi + g_W^e\phi - \lambda\phi = 0,$$

$$\Delta_\lambda \equiv \frac{\kappa}{2}\left[A(1 + z)\cosh(\Omega_\lambda L) + B(1 - z)\sinh(\Omega_\lambda L)\right] - \kappa. \tag{4.11}$$

By writing (4.11) in matrix form, and then using (4.9) together with (4.7) for z, we readily derive, after some algebra, that the the discrete eigenvalues λ satisfy the transcendental equation $\mathcal{F}(\lambda) = 0$, where

$$\mathcal{F}(\lambda) \equiv \frac{1}{\Delta_\lambda} + \frac{g_W^e - \lambda}{\det(J_e - \lambda I)}, \tag{4.12a}$$

14

and where for each possible mode l of instability, with $l = 0, \ldots, m-1$, we have

$$\Delta_\lambda \equiv \frac{\kappa^2 \Omega_\lambda D \left[\mathrm{Re}(z_l) - \cosh\left(2\Omega_\lambda L\right)\right] - \kappa \Omega_\lambda^2 D^2 \sinh\left(2\Omega_\lambda L\right)}{\left(\Omega_\lambda^2 D^2 + \kappa^2\right) \sinh\left(2\Omega_\lambda L\right) + 2\kappa D\Omega_\lambda \cosh\left(2\Omega_\lambda L\right)}, \qquad \mathrm{Re}(z_l) = \cos\left(\frac{2\pi l}{m}\right). \qquad (4.12\mathrm{b})$$

Here J_e is the Jacobian of the reaction kinetics, as defined in (3.5a), evaluated at the steady-state (4.4).

Our goal below is to determine Hopf bifurcation thresholds for which $\mathcal{F}(\pm i\lambda_I) = 0$ in (4.12a), for some $\lambda_I > 0$. Such pure imaginary eigenvalues depend on $\mathrm{Re}(z)$ through Δ_λ, as defined in (4.12b). To examine the possible modes of instability, we observe that if z_l is one of the m-th roots of unity, then

$$z_l = \bar{z}_{m-l}, \quad l = 1, \ldots, \left\lfloor \frac{m}{2} \right\rfloor, \qquad (4.13)$$

where the floor function $\lfloor x \rfloor$ is defined as the largest integer not greater than x. Therefore, if m is odd, there are $(m+1)/2$ different values of $\mathrm{Re}(z)$, and thus $(m+1)/2$ different possible modes of linear instability. Alternatively, if m is even, there are $\frac{m}{2} + 1$ different possible modes of linear instability. The eigenvalue of multiplicity one corresponds to $z = 1$ (and also $z = -1$ if m is even). The remaining eigenvalues always have multiplicity two. In other words, the eigenvalue corresponding to z_l is also an eigenvalue for $z = z_{m-l}$. Therefore, if we find a Hopf bifurcation point for $z \neq \pm 1$, then there are always two possible spatial modes of oscillation for that specific pair of purely imaginary eigenvalues. Finally, to determine the predicted spatial pattern of any Hopf bifurcation point $\lambda = i\lambda_I$, we observe that at the midpoint between the cells the perturbation $\mathrm{Re}(e^{\lambda t}\eta\left[(2j-1)L\right])$ to the bulk diffusion field $C(x,t)$ is

$$\mathrm{Re}\left(e^{i\lambda_I}\eta\left[(2j-1)L\right]\right) = \cos\left(\lambda_I t + \frac{2\pi l j}{m}\right), \quad j = 0, \ldots, m. \qquad (4.14)$$

4.3 Hopf Bifurcation Boundaries, Global Branches and Numerics

Next, we use (4.12) to compute the Hopf bifurcation boundaries for the different possible modes of instability in the D versus κ parameter plane. We remark that the choice $l = 0$ in (4.12) corresponds to in-phase synchronous perturbations across the cells, whereas the $\lfloor \frac{m}{2} \rfloor$ other eigenvalues correspond to the various anti-phase modes across the m cells. For $m = 3$, and for one particular parameter set for the Sel'kov model (2.1c), in Fig. 7 we plot the Hopf bifurcation thresholds in the D versus κ plane.

Next, for the $m = 3$ cell problem with $\kappa = 1$, we use XPPAUT [4] to compute the global bifurcation diagram, as a function of D, for the in-phase synchronous periodic solution branch, which bifurcates from the symmetric steady-state solution in (4.4) at the two distinct values of D shown in the left panel of Fig. 7. The computations, done by first discretizing (4.1), are displayed in the left panel of Fig. 8. From this figure we observe that for larger values of D the in-phase synchronous periodic solution branch is linearly stable, but it then destabilizes as D is decreased towards the lower Hopf bifurcation threshold.

To verify the linear stability properties of the steady-state solution for the $l = 0$ and $l = 1, 2$ modes off of the Hopf bifurcation boundaries, we can use a similar winding number criterion for $\mathcal{F}(\lambda)$, defined in (4.12), as was developed in §3.2. With the same notation as in §3.2, the number N of unstable eigenvalues of the linearization of the symmetric steady-state for the periodic cell problem is

$$N = \frac{1}{\pi}[\arg \mathcal{F}]\Big|_{\Gamma_{I_+}} + P, \qquad P = \begin{cases} 2, & \text{when} \quad \mathrm{tr}(J_e) > 0, \\ 0, & \text{when} \quad \mathrm{tr}(J_e) < 0. \end{cases} \qquad (4.15)$$
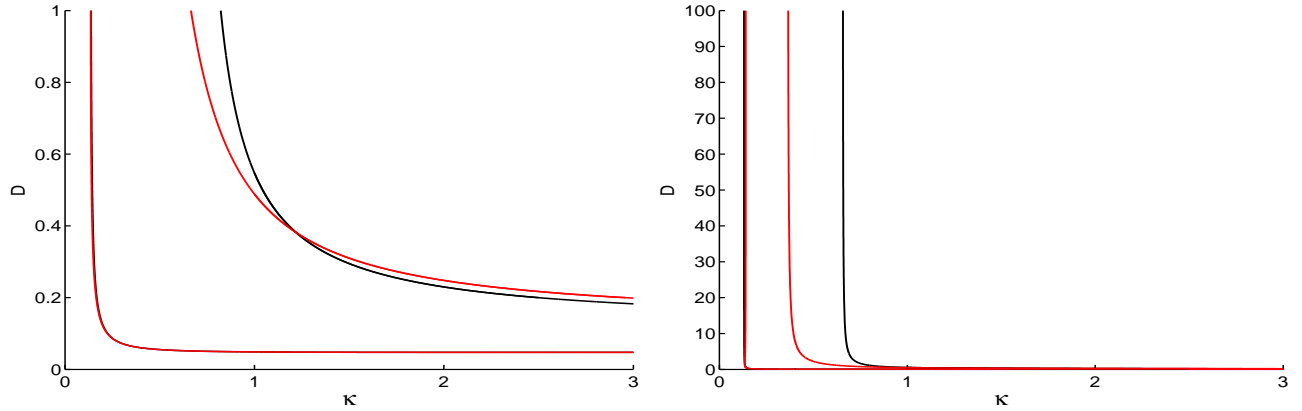
Figure 7: Left: Phase diagram showing Hopf bifurcation boundaries for the case of three $(m = 3)$ cells in the D versus κ plane for $k = 1$, $L = 1$, and where the Sel'kov parameters in (2.1c) are $\epsilon = 0.15$, $\mu = 2$ and $\alpha = 0.9$. The black curves corresponds to $l = 0$ and the red curves corresponds to $l = 1, 2$. The black and red curves almost coincide on the lower boundary. In the region bounded by the two black and two red curves the symmetric steady-state is linearly unstable to the $l = 0$ and $l = 1, 2$ modes, respectively. Right: Same as the left panel, but with a larger range of D for the vertical axis. For these parameter values we observe that the region of instability is unbounded in the D versus κ plane.
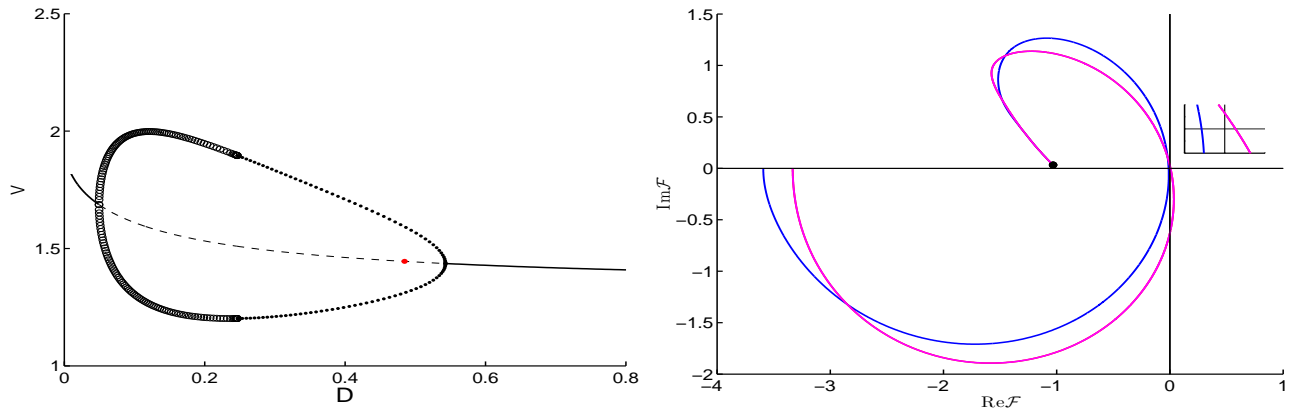

Figure 8: Left: Global bifurcation diagram with $m = 3$ cells on the domain $[-1, 5]$ for $\kappa = 1$, with the other parameters as in the caption of Fig. 7. The solid and dashed lines denote linearly stable and unstable branches of steady-state solutions, respectively. The closed loop is the global branch of in-phase synchronous periodic solutions. The upper Hopf bifurcation value $D \approx 0.54299$ is for the $l = 0$ in-phase mode. The solid/open circles on this loop denotes a linearly stable/unstable periodic solution, respectively. The red dot at $D \approx 0.48482$ corresponds to the Hopf bifurcation point for the degenerate $l = 1, 2$ mode. Right panel: Plot of $\mathcal{F}(i\lambda_I)$ as λ_I decreases from 1000 to 0 with $D = 0.5$. The blue curve corresponds to $l = 0$, and the magenta curve is for $l = 1, 2$. The inner panel shows the curves near the origin. The trace and determinant of J_e are $\mathrm{tr} J_e = 0.4879$ and $\det J_e = 0.4474$, so that $P = 2$ in (4.15). We obtain $N = 2$ unstable eigenvalues for $l = 0$, and $N = 0$ for $l = 1, 2$ from (4.15).

16

For $\kappa = 1$ and $D = 0.5$, a numerical computation of the winding number shown in the right panel of Fig. 8 yields $\left[\arg \mathcal{F}\right]\Big|_{\Gamma_{I_+}} = 0$ for $l = 0$ and $\left[\arg \mathcal{F}\right]\Big|_{\Gamma_{I_+}} = -2\pi$ for $l = 1, 2$. Therefore, $N = 2$ for $l = 0$ and $N = 0$ for $l = 1, 2$. These results agree with those predicted from the phase diagram in the left panel of Fig. 7, since it is only the in-phase $l = 0$ mode that is within the region of instability.
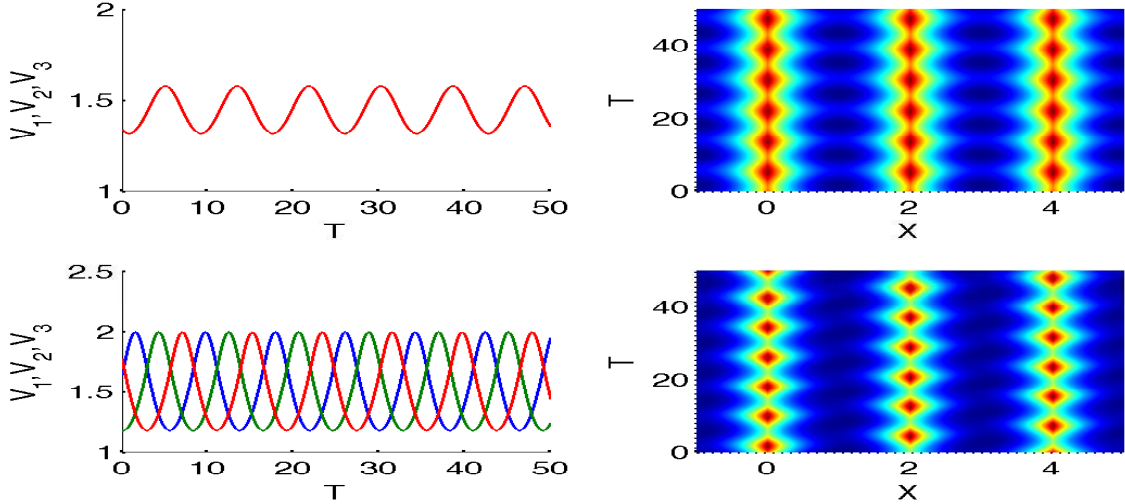

Figure 9: Full numerical results computed from (4.1) with $D = 0.5$ (upper row) and $D = 0.2$ (lower row). Other parameters are the same as in Fig. 7 with $\kappa = 1$. The initial conditions for $D = 0.5$ are $V_0 = [0.5, 1.5, 0.5]$, $W_0 = [1, 1, 1]$, and $C_0(x) = 1$. For $D = 0.2$ the initial conditions are $V_0 = [0.5, 1.5, 0.5]$, $W_0 = [1, 1, 1]$, and $C_0(x) = 1$ if $x > 0$, $C_0(x) = \sin(x) + 1$ if $x < 0$. The V_1, V_2 and V_3 curves are in blue, green and red respectively. For $D = 0.5$ there are stable in-phase synchronous oscillations, whereas for $D = 0.2$ stable phase-shifted synchronous oscillations occur. The phase shift among V_1, V_2 and V_3, is consistent with the mode $l = 2$ in the linear stability analysis (4.14). The right panel in each row is a contour plot of $C(x, t)$.

Finally, to confirm predictions obtained from the linear stability analysis and the global bifurcation diagram, full time-dependent numerical solutions of the coupled PDE-ODE system (4.1) were computed for two values of D when $\kappa = 1$ by using a method of lines approach based on a second-order spatial discretization for the bulk diffusion. In the upper row in Fig. 9 for $D = 0.5$ we observe, as expected, a stable in-phase synchronous periodic solution. In the lower row of Fig. 9 where $D = 0.2$, the full numerical simulations show a stable asynchronous oscillation where the dynamics in the cells are phase-shifted. The phase-shifting observed in the lower row of Fig. 9 is consistent with the $l = 2$ mode (with $m = 3$) in the result (4.14) from the linear stability analysis, in that the bulk diffusion field at the midpoint of the cells and the cell dynamics V_1, V_2, V_3 have the form $\cos(\lambda_I t)$, $\cos(\lambda_I t + 4\pi/3)$, and $\cos(\lambda_I t + 8\pi/3)$.

4.4 Large D Analysis for the Hopf Bifurcation Boundaries

In this subsection, we examine analytically some qualitative aspects of the region in the D versus κ phase diagram shown in Fig. 7 where the symmetric steady-state is linearly unstable. In particular, we will

17

study the large D behavior of the Hopf bifurcation boundaries in this plane. From this analysis we will also formulate a simple criterion that can be used to predict whether the lobe of instability in the D versus κ plane is bounded in D for other domain lengths L and bulk degradation parameter k. For the choice $L = k = 1$ the instability regions were unbounded as $D \to \infty$ (see the right panel of Fig. 7).

Firstly, we determine the limiting behavior of $\mathcal{F}(\lambda)$ in (4.12) as $D \to \infty$. Upon using $\Omega_\lambda D \sinh(2\Omega_\lambda L) \sim 2\Omega_\lambda^2 LD = 2(k + \lambda)L$ and $\cosh(2\Omega_\lambda L) \sim 1$, we obtain from (4.12b) that

$$\lim_{D \to \infty} \Delta_\lambda = \Delta_{\lambda,\infty} \equiv \frac{\kappa^2(Re(z_l) - 1) - 2\kappa L(k + \lambda)}{2L(k + \lambda) + 2\kappa}. \tag{4.16}$$

Therefore, $\mathcal{F}(\lambda)$ in (4.12a) has the following limiting form as $D \to \infty$:

$$\lim_{D \to \infty} \mathcal{F}(\lambda) \equiv \mathcal{F}_\infty(\lambda) \equiv \frac{1}{\Delta_{\lambda,\infty}} + \frac{g_W^e - \lambda}{\det(J_e - \lambda I)}. \tag{4.17}$$

In addition, for $D \to \infty$, we can also find an approximate expression for the steady state V^e from (4.4c), which is needed to calculate the terms in (4.17). By using $D\omega \tanh(\omega L) \sim D\omega^2 L \sim kL$, we obtain from (4.4c), that for $D \to \infty$,

$$\lim_{D \to \infty} V^e = V_\infty^e \equiv \frac{\mu(\kappa + Lk)}{\kappa + (1 + \kappa)kL}, \qquad \lim_{D \to \infty} W^e = W_\infty^e \equiv \frac{\mu}{\alpha + (V_\infty^e)^2}. \tag{4.18}$$

We observe from (4.16), (4.17) and (4.18), that upon setting $\mathcal{F}_\infty(\lambda) = 0$, and rearranging the resulting expression, we obtain a cubic equation in λ of the form

$$\lambda^3 + \lambda^2 p_1 + \lambda p_2 + p_3 = 0, \tag{4.19a}$$

where we have identify p_1, p_2 and p_3 by

$$p_1 \equiv \frac{a}{2L} + \kappa - \text{tr}(J_e), \qquad p_2 \equiv \det(J_e) - \kappa g_W^e - \frac{(a\,\text{tr}(J_e) + b)}{2L}, \qquad p_3 \equiv \frac{(a\det(J_e) + bg_W^e)}{2L}, \tag{4.19b}$$

and where we have defined a and b by

$$a \equiv 2(\kappa + kL), \qquad b \equiv \kappa^2(\text{Re}(z_l) - 1) - 2L\kappa k. \tag{4.19c}$$

Next, we simplify (4.19b) for the Sel'kov kinetics (2.1c), for which

$$\det(J_e) = \epsilon\left(\alpha + (V_\infty^e)^2\right) = -g_W^e > 0, \qquad \text{tr}(J_e) = 2V_\infty^e W_\infty^e - 1 - \det(J_e). \tag{4.20}$$

By substituting (4.20) into (4.19b), we readily calculate that

$$p_1 \equiv \kappa\left(1 + \frac{1}{L}\right) + k + 1 + \det(J_e) - \frac{2\mu V_\infty^e}{\left(\alpha + (V_\infty^e)^2\right)},$$

$$p_2 \equiv \left(1 + \kappa\left(1 + \frac{1}{L}\right) + k\right)\det(J_e) + \frac{\xi}{2L} - \frac{2(\kappa + kL)\mu V_\infty^e}{L\left(\alpha + (V_\infty^e)^2\right)}, \tag{4.21}$$

$$p_3 \equiv \frac{\xi}{2L}\det(J_e), \qquad \xi \equiv a - b = 2kL(1 + \kappa) + 2\kappa + \kappa^2(1 - \text{Re}(z_l)) > 0.$$
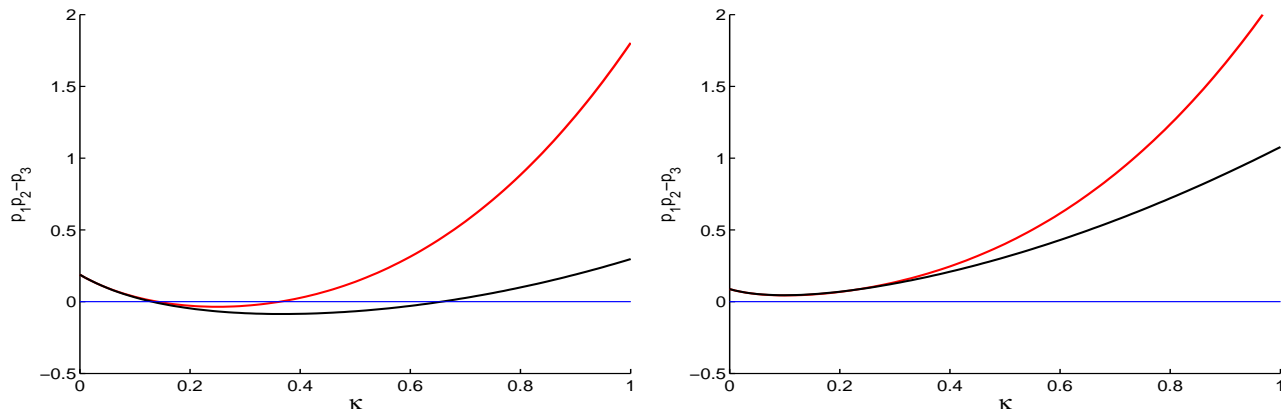
18

Figure 10: Plot of $p_1 p_2 - p_3$ versus κ for $l = 0$ (black) and $l = 1$ (red) for a ring of $m = 3$ cells. The blue horizontal line is the threshold $p_1 p_2 = p_3$. Any intersections of the black (red) curve with the blue line yields the bifurcation points for κ for $l = 0$ ($l = 1$). Left panel: the parameter values as given in Fig. 7. Between the two bifurcation points, the black (red) curve lies below the threshold $p_1 p_2 = p_3$, and so by the Routh-Hurwitz criterion there are unstable eigenvalues. Numerically we verify $p_1 > 0$. Right panel: same parameters except that now the bulk decay is smaller at $k = 0.3$. There are now no Hopf bifurcation values of κ in the $D \to \infty$ regime.

For the Sel'kov model with $\epsilon = 0.15$, $\mu = 2$, and $\alpha = 0.9$, we now use the cubic (4.19a) with coefficients (4.21) to calculate the the limiting Hopf bifurcation values of κ, valid as $D \to \infty$, when $k = 1$ and $L = 1$. By the *Routh-Hurwitz* criterion, a necessary and sufficient condition for all of the roots of (4.19a) to satisfy $Re(\lambda) < 0$ is that the following three inequalities hold:

$$p_1 > 0, \qquad p_3 > 0, \qquad p_1 p_2 > p_3 . \tag{4.22}$$

From (4.21), we have $p_3 > 0$ for any parameter set. Moreover, the Hopf bifurcation boundary satisfies

$$p_1 p_2 = p_3 . \tag{4.23}$$

provided that $p_1 > 0$ and $p_3 > 0$.

Our numerical computations, from enforcing (4.23) for $m = 3$, predict that there is a Hopf bifurcation for $D \gg 1$ when

$$l = 0, \quad \kappa \approx 0.1313 \text{ and } 0.6564 ; \qquad l = 1, \quad \kappa \approx 0.1407 \text{ and } 0.3633 . \tag{4.24}$$

This is shown in Fig. 10. In contrast, from the phase diagram of D versus κ, as seen in the right panel of Fig. 7, we obtain for $D = 100$ that the Hopf bifurcation values for κ are

$$l = 0, \quad \kappa \approx 0.1314 \text{ and } 0.6579 ; \qquad l = 1, \quad \kappa \approx 0.1405 \text{ and } 0.3665 , \tag{4.25}$$

which are remarkably close to the values calculated in (4.24) from the $D \to \infty$ theory.

Finally, to obtain a bounded lobe of instability in the D versus κ plane, rather than the unbounded region as $D \to \infty$ shown in Fig 7, all that is needed is to seek conditions on the domain length L and

19

bulk parameter k such that the Routh-Hurwitz stability condition (4.22) holds for all κ. This can be achieved by decreasing either L or k. We remark that if we decrease either the domain length L or bulk decay parameter k, then the black and red curves in Fig. 10 move up, and so there no longer any Hopf bifurcation points for the $D \to \infty$ regime. An example of this is shown in the right panel of Fig. 10 for the same parameters as in the left panel of Fig 10 except that now $k = 0.3$. In this case, the instability lobe in the phase diagram of D versus κ would be bounded in D for both the $l = 0$ and $l = 1, 2$ modes.

5 Nonlinear Coupling Between Compartments and Bulk

In §3 we considered the case where there is a linear coupling between the compartment and the bulk. Such a linear coupling term shifts the steady-state of the original ODE system from $V_e = \mu$ to a new value that depends on the coupling strength β, which ultimately yields bifurcating branches of periodic solutions through a Hopf bifurcation along the steady-state solution branch. In this section we briefly examine an alternative scenario for the creation of compartmental-bulk oscillations. More specifically, we will study a particular nonlinear coupling between the compartments and the bulk that possesses the same stable steady-state as that of the uncoupled ODE system in the compartment, but that still has the effect of generating compartment-bulk oscillations. In this model, the nonlinear coupling leads to the creation of branches of periodic solutions exhibiting saddle-node behavior, which are disconnected from the steady-state solution branch.

To illustrate such a possibility, we choose the coupling term $P(C(2Li, t), V)$, for $i = 0, 1$, as

$$
P(C(2Li, t), V) = h(C(2Li, t))q(V(t)),
$$
$$
h(C(2Li, t)) = \frac{C(2Li, t)(C(2Li, t) - c_0)}{K_c + C(2Li, t)^2}, \quad q(V) = \frac{V(V - \mu)}{L_v + V^2}, \quad i = 0, 1,
$$
(5.1)

where $L_v > 0$, $K_c > 0$, and where we have defined c_0 by

$$
c_0 = \gamma\mu, \qquad \gamma \equiv \frac{\kappa}{\kappa + D\omega \tanh(\omega L)}, \qquad \omega \equiv \sqrt{k/D}.
$$
(5.2)

As in §3 we will determine the symmetric steady-state solution to (2.1) with (5.1) and analyze its linear stability. Upon solving the time-independent problem for (2.1) on the domain $[0, L]$, with no-flux boundary condition for C at $x = L$, we readily obtain that

$$
C_e(x) = C_e^0 \frac{\cosh(\omega(L - x))}{\cosh(\omega L)}, \qquad C_e^0 = \frac{\kappa V_e}{\kappa + D\omega \tanh(\omega L)}, \qquad W_e = \frac{\mu}{\alpha + V_e^2},
$$
(5.3)

where V_e satisfies the following fifth order polynomial:

$$
(V_e - \mu)Q(V_e) = 0, \qquad Q(V_e) \equiv V_e^4 - \beta V_e^3 + V_e^2 \left(\frac{K_c}{\gamma^2} + L_v + \beta\mu \right) + \frac{K_c L_v}{\gamma^2}.
$$
(5.4)

Here γ and ω are defined in (5.2). We observe that with the nonlinear coupling function (5.1), the steady-state solution of the uncoupled ODE compartmental dynamics is still a steady-state of the coupled ODE system. Specifically, we have the uncoupled steady-state

$$
V_e = \mu, \qquad W_e = \frac{\mu}{\alpha + \mu^2}, \qquad C_e^0 = c_0,
$$
(5.5)

20

which corresponds to setting $\beta = 0$ in (3.2). In addition, there can be at most four other steady-state solutions, corresponding to the roots of $Q(V_e) = 0$ in (5.4). However, since $Q(\mu) > 0$, none of these additional steady-state solution branches bifurcate from the uncoupled steady-state branch (5.5).

To examine the stability of the steady-state (5.5), we introduce the same perturbation as in (3.3). Upon linearizing (2.1), we obtain, after some algebra, that the associated eigenvalue λ satisfies

$$\lambda^2 - \lambda(g_W^e + f_V^e + \beta(P_V^e + \delta P_C^e)) + (g_W^e f_V^e - g_V^e f_W^e + \beta g_W^e (P_V^e + \delta P_C^e)) = 0,$$

where

$$\delta \equiv \frac{\kappa}{\kappa + D\Omega_\lambda \tanh(\Omega_\lambda L)}, \quad \text{(in-phase)}, \qquad \text{or} \qquad \delta \equiv \frac{\kappa}{\kappa + D\Omega_\lambda \coth(\Omega_\lambda L)}, \quad \text{(anti-phase)}.$$

We observe that with the special choice (5.1) of nonlinear coupling $P(C(0, t), V)$, we have $P_C^e = 0$ and $P_V^e = 0$, so that the characteristic equation for λ becomes

$$\lambda^2 - \lambda(g_W^e + f_V^e) + (g_W^e f_V^e - g_V^e f_W^e) = 0,$$

which is the same as that for the uncoupled problem. Since we assumed that the uncoupled problem has stable dynamics, we have $\text{Re}(\lambda) < 0$. Thus, our linear stability analysis predicts that the steady-state (5.5) can never be destabilized by the nonlinear coupling (5.1).

To determine whether, nevertheless, there can be any compartment-bulk oscillations, we used XP-PAUT [4] to compute global bifurcation diagrams after first spatially discretizing (2.1) with the coupling (5.1). In Fig. 11 we show two typical bifurcation diagrams of the compartmental variable V. In the left panel of Fig. 11 we plot V versus the coupling strength β for the fixed diffusivity $D = 0.1$ showing the stable steady-state solution and the branch of in-phase synchronous periodic oscillations. There is also a branch of anti-phase periodic solutions (not shown), that essentially overlaps the in-phase branch. This overlap occurs since for $D = 0.1$, the bulk diffusion field decays rather quickly away from $x = 0$ and $x = 2L$, which leads to a rather weak coupling between the two compartments. The key feature from the left panel of Fig. 11 is that there is some parameter regime in β, with $D = 0.1$, where stable in-phase synchronous time-periodic solutions co-exist with the stable steady-state solution (5.5). This phenomenon cannot be revealed from a local linear stability analysis along the solution branch (5.5). For $\beta = 4$, in the right panel of Fig. 11 we plot a bifurcation diagram of V versus D showing the stable steady-states together with disconnected branches of in-phase and anti-phase periodic solutions. Both the anti-phase and in-phase synchronous branches have a saddle-node bifurcation point at $D \approx 0.57$ and $D \approx 0.67$, respectively. The in-phase branches are always unstable. Stable anti-phase time-periodic solutions co-exist with the stable steady-state solution (5.5) when $D < 0.57$. As a result of the saddle-node structure, seen in the right panel of Fig. 11, it is clear that the coupled system will yield hysteretic behavior under a slow periodic sweep in the diffusivity D.

To confirm predictions from the bifurcation diagram, we computed full numerical solutions of the PDE-ODE system (2.1) with the nonlinear coupling (5.1) for $D = 0.5$ and $\beta = 4$, with the other parameter values as given in the caption of Fig. 12. From Fig. 11, we observe for these parameter values that the anti-phase mode is stable. The full numerical results shown in Fig. 12 confirm this prediction of stable anti-phase oscillatory dynamics.
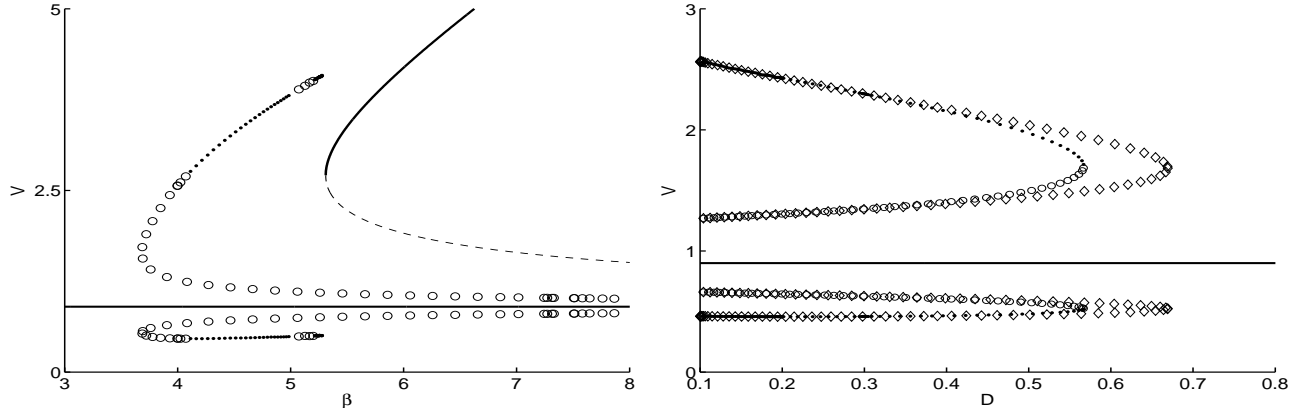
Figure 11: Bifurcation diagram of the local variable V with respect to the coupling strength β and diffusivity D for the parameter set $L = 1$, $k = 2$, $\kappa = 3$, $\epsilon = 0.15$, $\mu = 0.9$, $\alpha = 0.55$, $K_c = 1$ and $L_v = 0.8$. The solid/dashed line represents stable/unstable steady-state solutions of V, open/solid circle indicate unstable/stable periodic solutions branches, respectively. The steady-state (5.5) is the solid horizontal line. Left panel: V versus β for $D = 0.1$. The periodic solution branches shown correspond only to the in-phase oscillations. Stable in-phase synchronous oscillations and stable steady-states will co-exist only for some range of β. Right panel: V versus D for $\beta = 4$. The periodic solution branch that is unstable, with a saddle-node point at $D \approx 0.67$, is the in-phase branch. The other periodic solution branch, with a saddle-node point at $D \approx 0.57$ represents anti-phase oscillations. This plot shows that in-phase oscillations are unstable for $\beta = 4$, but that stable anti-phase oscillations and stable steady-state solutions will co-exist in some range of D when $\beta = 4$.

5.1   Compartmental Dynamics Neglecting Bulk Diffusion

As shown above, a local stability analysis around the steady-state (5.5) does not provide any insight into the occurrence of oscillatory behavior of the coupled PDE-ODE system (2.1) with coupling (5.1). In this subsection, we consider an ODE model in the compartment, where we have neglected the bulk diffusion process, and simply set $P(C, V) = q(V)$ in (5.1). The resulting ODE model is written as

$$\frac{dV}{dt} = f_0(V, W) - V + \beta q(V), \qquad \frac{dW}{dt} = \epsilon(\mu - f_0(V, W)),$$

$$f_0(V, W) \equiv \alpha W + WV^2, \qquad q(V) \equiv \frac{V(V - \mu)}{L_v + V^2}. \tag{5.6}$$

A typical bifurcation diagram of this ODE system, computed numerically, is shown in Fig. 13. From this figure we observe that there are three types of critical points; three Hopf bifurcation (HB) points, the saddle node (SN) point, and the transcritcal point (IS) where two steady-state branches intersect.

To determine the location of these points we first determine the steady-states of (5.6), which satisfy

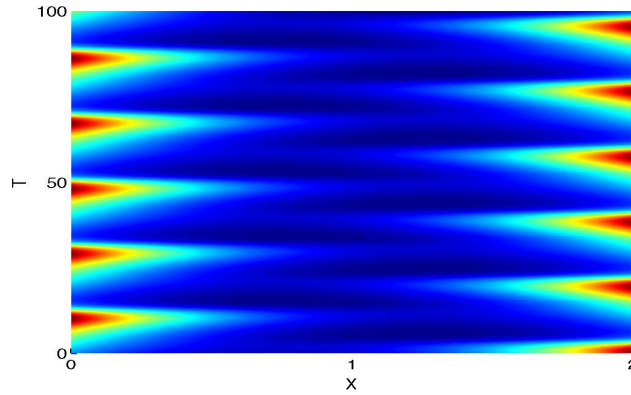$$(V_e - \mu)(V_e^2 - \beta V_e + L_v) = 0. \tag{5.7}$$

22

Figure 12: Numerical simulation of the coupled PDE-ODE system (2.1) with the nonlinear coupling (5.1) for $D = 0.5$, $\beta = 4$, and $L = 1$. The other parameter values are the same as in the caption of Fig. 11. The initial conditions are $C(x,0) = 2$, $v_1 = 1$, $w_1 = 0.3$, $v_2 = 0.2$, and $w_2 = 0.3$. Stable anti-phase oscillations for $C(x,t)$ are observed.
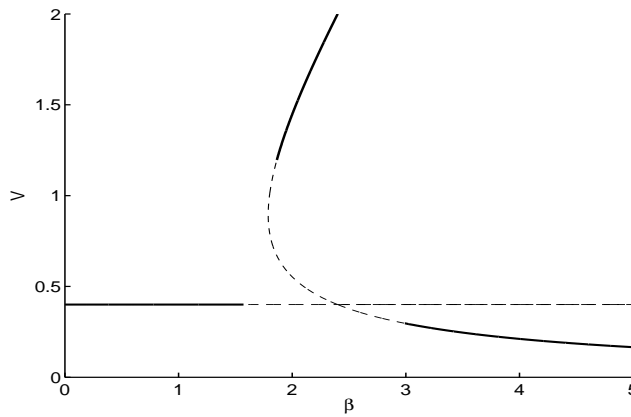

Figure 13: Bifurcation diagram of the ODE system (5.6) versus β for the parameter set $\epsilon = 0.15$, $\mu = 0.4$, $\alpha = 0.55$, and $L_v = 0.8$. The solid/dashed line represents stable/unstable steady-state solutions of V.

23

Therefore, $V_e = \mu$ is a steady-state, and there are two additional steady-state solutions given by

$$V_e^{\pm} = \frac{\beta}{2} \pm \sqrt{\left(\frac{\beta}{2}\right)^2 - L_v}\,, \tag{5.8}$$

when $L_v < \beta^2/4$. At the SN point, we have $V_e^+ = V_e^-$, which gives

$$\beta_{\mathrm{SN}} = 2\sqrt{L_v}\,, \qquad \text{and} \qquad V_e^{\pm} = \sqrt{L_v}\,. \tag{5.9}$$

For the parameter values in Fig. 13 we get $\beta_{\mathrm{SN}} \approx 1.789$.

At the IS point, since one of $V_e^{\pm}$ must equal μ, we obtain that

$$\frac{\beta}{2} \pm \sqrt{\left(\frac{\beta}{2}\right)^2 - L_v} = \mu\,, \tag{5.10}$$

which yields $\beta = \mu + L_v/\mu$. Since, $\mu - \beta/2 = (\mu^2 - L_v)(2\mu)$, we conclude that $V_e^- = \mu$ when $L_v > \mu^2$, and $V_e^+ = \mu$ when $L_v < \mu^2$. The parameter set in the caption of Fig. 13 corresponds to this first possibility. The IS point occurs at $\beta_{\mathrm{IS}} = \left(0.4^2 + 0.8\right)/0.4 = 2.4$.

To determine the HB points, we calculate the trace and the determinant of the Jacobian matrix J_e associated with (5.6) as

$$\mathrm{tr}(J_e) = f_{0V}^e - 1 + \beta q'(V_e) - \epsilon f_{0W}^e\,, \qquad \det(J_e) = -\epsilon f_{0W}^e \left(\beta\, q'(V_e) - 1\right)\,.$$

The Hopf bifurcation occurs when $\mathrm{tr}(J_e) = 0$ and $\det(J_e) > 0$, which gives

$$\beta q'(V_e) = 1 + \epsilon f_{0W}^e - f_{0V}^e\,, \tag{5.11a}$$

provided that

$$\det(J_e) = -\epsilon f_{0W}^e (\epsilon f_{0W}^e - f_{0V}^e) = \epsilon \left[2V_e\mu - \epsilon\left(\alpha + V_e^2\right)^2\right] > 0\,. \tag{5.11b}$$

To determine the HB point off of the $V_e = \mu = 0.4$ steady-state branch in Fig. 13, we set $V_e = \mu$ in (5.11b) to calculate that $\det(J_e) \approx 0.0367 > 0$. By using (5.6) for $q(V)$ to calculate $q'(\mu)$, we obtain from (5.11a) that the HB point β_{HB} is

$$\beta_{\mathrm{HB}} = \frac{(L_v + \mu^2)}{\mu(\alpha + \mu^2)} \left[\alpha - \mu^2 + \epsilon(\alpha + \mu^2)^2\right]\,. \tag{5.12}$$

For the parameter set of Fig. 13 this yields $\beta_{\mathrm{HB}} \approx 1.574$. The other two HB points in Fig. 13, corresponding to bifurcations from the $V_e^{\pm}$ steady-states, are also readily calculated from (5.11). We find that the Hopf bifurcation on the v_+ branch is at $\beta_{\mathrm{HB}} \approx 1.8641$ with $\det(J_e) \approx 0.0554 > 0$, while the Hopf bifurcation on the v_- branch occurs at $\beta_{\mathrm{HB}} \approx 2.9884$ with $\det(J_e) \approx 0.0265 > 0$.

We conclude that the bifurcation diagram of the ODE system (5.6) does share only a few of the characteristics observed in the bifurcation diagram of Fig. 11 for the fully coupled compartmental-bulk problem (2.1) with (5.1). For both the ODE model and the fully coupled PDE-ODE model, new branches of steady-state solutions, other than the base-state $V_e = \mu$, are possible. However, for the fully coupled problem, the branches of periodic solutions are isolated in the sense that they do not arise from bifurcations off of the steady-state solution branches.

6 Discussion

On a one-dimensional spatial domain, we have introduced and analyzed a PDE-ODE model that couples two dynamically active compartments, separated spatially by a distance $2L$, through a linear bulk diffusion field. For this relatively new paradigm for diffusive coupling, we have used linear stability theory and numerical bifurcation software to show that bulk diffusion can trigger a stable in-phase synchronous oscillatory instability in the temporal dynamics associated with the two active compartments. We have also extended the basic two-compartment analysis to determine Hopf bifurcation thresholds for a periodic chain of dynamically active units that are linearly coupled to a bulk diffusion field. Although, for concreteness, we have used a simple Sel'kov dynamics for the reaction-kinetics in the two compartments, the mechanism through which oscillatory dynamics occur will be similar for other kinetics.

A biologically relevant direction that warrants further investigation is to introduce different, more detailed, models for the coupling strength between the compartment and the bulk. As we have shown for our linearly coupled model in §3, stable synchronized oscillations can occur only for some range of the coupling strength β and diffusivity D. It would be interesting to analyze triggered oscillations that result when the compartment-bulk coupling strength β varies dynamically in time, or is coupled to some slow dynamics, so as to create periodic bursts of synchronous oscillatory behavior, followed by intervals of quiescent behavior, in the two compartments. Such bursting and triggered dynamics have been well-studied in a purely ODE context (cf. [1], [2], [11], see also the reference therein). A related, but rather challenging direction, would be to investigate the possibility of synchronized oscillations when β is allowed to switch stochastically in time between two constant states, representing an ON or OFF state that are either inside or outside the parameter region for oscillations shown in Fig. 1, respectively. Such stochastic switching behavior is a characteristic feature of channels in biological membranes. The resulting model is a stochastic hybrid system that consists of both continuous PDE-ODE dynamics, punctuated by discrete stochastic events. A mathematical analysis of a class of related stochastic hybrid system, whereby the boundary condition for a heat equation on a finite domain switches randomly between Dirichlet and Neumann, is analyzed in [13].

Finally, it would be interesting to extend our analysis to quorum-sensing problems in multiple spatial dimensions, such as in the case study [17], whereby reaction-kinetics occur within spatially localized compartments and where a diffusing signalling molecule mediates a communication between the spatially segregated compartments. Some work in this direction is given in [10].

A The Winding Number Analysis

In this appendix we use the argument principle of complex analysis to determine an expression for the number N of roots of $\mathcal{F}(\lambda) = 0$ in $\operatorname{Re}(\lambda) > 0$ of the spectral plane, where $\mathcal{F}(\lambda)$ is defined in (3.5).

To do so, we calculate the winding number of $\mathcal{F}(\lambda)$ over the contour consisting of the imaginary axis $-iR \leq \mathrm{Im}\lambda \leq iR$, decomposed as $\Gamma_{I_+} = i\lambda_I$ and $\Gamma_{I_-} = -i\lambda_I$ where $0 < \lambda_I < R$, together with the semi-circle $|\lambda| = R$, with $|\arg\lambda| \leq \pi/2$, which we denote by Γ_R. Assuming that there are no roots of $\mathcal{F}(\lambda) = 0$ on the imaginary axis, we use the argument principle to determine N as

$$N = \frac{1}{2\pi}\left(\lim_{R\to\infty}[\arg\mathcal{F}]_{\Gamma_R} + 2\lim_{R\to\infty}[\arg\mathcal{F}]_{\Gamma_{I_+}}\right) + P\,, \tag{A.1}$$

where P is the number of poles of $\mathcal{F}(\lambda)$ in $\mathrm{Re}(\lambda) > 0$. Here $[\arg\mathcal{F}]_\Gamma$ denotes the change in the argument of $\mathcal{F}(\lambda)$ over the contour Γ oriented in the counterclockwise direction. In deriving (A.1), we have used $\overline{\mathcal{F}(\lambda)} = \mathcal{F}(\bar{\lambda})$ to obtain the relation $\lim_{R\to\infty}[\arg\mathcal{F}]_{\Gamma_{I_-}} = \lim_{R\to\infty}[\arg\mathcal{F}]_{\Gamma_{I_+}}$.

To determine P, we first observe from (3.5) that the choice of the principal branch of the square root for Ω_λ ensures that $1/p_\pm(\lambda)$ is analytic in $\mathrm{Re}(\lambda) > 0$. Therefore, P is determined by the number of zeros of the quadratic $\det(J_e - \lambda I) = \lambda^2 - \mathrm{tr}(J_e)\lambda + \det(J_e)$ in $\mathrm{Re}(\lambda) > 0$. By using the specific forms of the nonlinearities $f(V, W)$ and $g(V, W)$ in (2.1c), we calculate $\det(J_e) = \epsilon(\alpha + V_e^2) > 0$. Therefore, in terms of the trace of J_e, denoted by $\mathrm{tr}(J_e)$, we have $P = 2$ if $\mathrm{tr}(J_e) > 0$ and $P = 0$ if $\mathrm{tr}(J_e) < 0$.

Next, we determine the change in the argument of $\mathcal{F}(\lambda)$ over Γ_R as $R \to +\infty$. Since $\det(J_e - \lambda I)$ is a quadratic function of λ and $1/p_\pm(\lambda) \sim \beta^{-1} + \mathcal{O}(\Omega_\lambda^{-1/2})$ as $|\lambda| \to +\infty$ in $\mathrm{Re}(\lambda) > 0$, we estimate from (3.5a) and (3.5b) that, for either the in-phase or anti-phase modes,

$$\mathcal{F}(\lambda) \sim \frac{1}{\beta} + \frac{\kappa}{D\Omega_\lambda\beta} + \mathcal{O}\left(\frac{1}{\lambda}\right)\,, \qquad \text{as} \quad |\lambda| = R \to +\infty\,, \tag{A.2}$$

where $|\arg\lambda| \leq \pi/2$. Hence, we have $\lim_{R\to\infty}[\arg\mathcal{F}]_{\Gamma_R} = 0$, so that (A.1) becomes

$$N = \frac{1}{\pi}\lim_{R\to\infty}[\arg\mathcal{F}]_{\Gamma_{I_+}} + P\,, \qquad P = \begin{cases} 2\,, & \text{when} \quad \mathrm{tr}(J_e) > 0\,, \\ 0\,, & \text{when} \quad \mathrm{tr}(J_e) < 0\,. \end{cases} \tag{A.3}$$

In this way, the problem of determining N is reduced to the simpler problem of calculating $[\arg\mathcal{F}]_{\Gamma_{I_+}}$ where Γ_{I_+} is traversed in the downwards direction. On Γ_{I_+}, we let $\lambda = i\lambda_I$ for $0 < \lambda_I < \infty$, and decompose $\mathcal{F}(i\lambda_I)$ in (3.5a) into real and imaginary parts as $\mathcal{F}(i\lambda_I) = \mathcal{F}_R(\lambda_I) + i\mathcal{F}_I(\lambda_I)$. As λ_I decreases from $+\infty$ to 0, we use (3.5a) to determine how many times $\mathcal{F}(i\lambda_I)$ wraps around the origin in the $(\mathcal{F}_R, \mathcal{F}_I)$ plane. By using (3.5b) to calculate the asymptotics of $p_\pm$ as $\lambda_I \to +\infty$, we conclude that $\mathcal{F}_R \to 1/\beta > 0$ and $\mathcal{F}_I \to 0$ as $\lambda_I \to +\infty$. This shows that $\arg\mathcal{F}(i\lambda_I) \to 0$ as $\lambda_I \to \infty$. In contrast, as $\lambda_I \to 0$, we further calculate from (3.5a) and (3.5b) that

$$\mathcal{F}(0) = \frac{1}{p_\pm(0)} - \frac{g_W^e}{\det(J_e)}\,, \qquad \text{where} \qquad \frac{1}{p_\pm(0)} = \begin{cases} \frac{1}{\beta} + \frac{\kappa}{\beta D\omega\tanh(\omega L)} > 0\,, \\ \frac{1}{\beta} + \frac{\kappa}{\beta D\omega\coth(\omega L)} > 0\,, \end{cases} \tag{A.4}$$

and $\omega \equiv \sqrt{k/D}$. Then, from the specific form of $g(V, W)$ in (2.1c), we get that $g_W^e = -\epsilon(\alpha + V_e^2) < 0$. Upon recalling that $\det(J_e) = \epsilon(\alpha + V_e^2) > 0$, we conclude from (A.4) that $\mathcal{F}(0) = [p_\pm(0)]^{-1} + 1 > 0$.

This indicates that as we traverse Γ_{I_+}, the path of $\mathcal{F}(i\lambda_I)$ both starts and ends on the positive real axis of the $(\mathcal{F}_R, \mathcal{F}_I)$ plane. It follows that the change in the argument of $\mathcal{F}(\lambda)$ on Γ_{I_+} can only be an integer number of 2π, so that $[\arg\mathcal{F}]\big|_{\Gamma_{I_+}} = 2m\pi$ for $m = 0, \pm 1, \pm 2, \ldots$. Consequently, (A.3) yields (3.6).

B   Formulation of the PDE-ODE System for a Periodic Chain

In this appendix we will derive (4.1b) for the local dynamics for the case of one cell on $[-L, L]$, which occupies a narrow interval $[-\epsilon, \epsilon]$ centered at the origin with $0 < \epsilon \ll 1$. Assume that the signaling molecule diffuses out of the cell at a certain rate. The local chemical species inside the cell, denoted by $\boldsymbol{u} = (u_1, u_2, \ldots, u_n)^T$, are assumed to satisfy the following system

$$\boldsymbol{u}_t = \epsilon D \boldsymbol{u}_{xx} + \boldsymbol{F}(\boldsymbol{u}), \qquad -\epsilon < x < \epsilon, \quad t > 0,$$
$$D\boldsymbol{u}_x(\epsilon, t) = \boldsymbol{e}_1 G_1(C(\epsilon, t), u_1(\epsilon, t)), \qquad D\boldsymbol{u}_x(-\epsilon, t) = \boldsymbol{e}_1 G_2(C(-\epsilon, t), u_1(-\epsilon, t)),$$
(B.1)

where $\epsilon \ll 1$ and $\boldsymbol{e}_1 = (1, 0, \ldots, 0)^T$. Here for simplicity we assume that all local chemicals share the same diffusivity $\epsilon D \ll 1$, with $D = \mathcal{O}(1)$, which is asymptotically small as compared to the reaction rate of the kinetics.

We now derive a reduced model from (B.1) in the limit $\epsilon \ll 1$ to obtain the approximate behavior of this system. To do so, we first introduce the local variable $y = \epsilon^{-1}x$, so that in terms of the y variable (B.1) becomes

$$\boldsymbol{u}_t = \epsilon^{-1} D \boldsymbol{u}_{yy} + \boldsymbol{F}(\boldsymbol{u}), \qquad -1 < y < 1, \quad t > 0,$$
$$D\boldsymbol{u}_y(1, t) = \epsilon \boldsymbol{e}_1 G_1(C(\epsilon, t), u_1(1, t)), \qquad D\boldsymbol{u}_y(-1, t) = \epsilon \boldsymbol{e}_1 G_2(C(-\epsilon, t), u_1(-1, t)).$$
(B.2)

We then expand the local specifies $\boldsymbol{u}$ as

$$\boldsymbol{u} = \boldsymbol{u}^0 + \epsilon \boldsymbol{u}^1 + \cdots.$$
(B.3)

Substituting this expansion into (B.2), and linearizing, we obtain to leading order that $\boldsymbol{u}^0$ satisfies

$$\boldsymbol{u}_{yy}^0 = 0, \quad -1 < y < 1; \qquad \boldsymbol{u}_y^0(\pm 1, t) = 0.$$
(B.4)

The solution to (B.4), which is independent of the spatial variable y, is $\boldsymbol{u}^0 = \boldsymbol{u}^0(t)$. We then proceed to the next order to determine the equation that $\boldsymbol{u}^0$ satisfies. At the next order, $\boldsymbol{u}^1$ satisfies

$$D\boldsymbol{u}_{yy}^1 = \boldsymbol{u}_t^0 - \boldsymbol{F}(\boldsymbol{u}^0), \quad -1 < y < 1,$$
$$D\boldsymbol{u}_y^1(1, t) = \boldsymbol{e}_1 G_1(C(\epsilon, t), u_1^0(t)), \qquad D\boldsymbol{u}_y^1(-1, t) = \boldsymbol{e}_1 G_2(C(-\epsilon, t), u_1^0(t)),$$
(B.5)

where $\boldsymbol{e}_1 = (1, 0, \ldots, 0)^T$, and u_1^0 denotes the first component of $\boldsymbol{u}^0$. For this $O(\epsilon)$ system, we invoke the divergence theorem to obtain that $\int_{-1}^{1} D\boldsymbol{u}_{yy}^1 \, dy = \int_{-1}^{1} (\boldsymbol{u}_t^0 - \boldsymbol{F}(\boldsymbol{u}^0)) \, dy$. Upon evaluating this expression, and using (B.5), we get

$$D\boldsymbol{u}_y^1(1, t) - D\boldsymbol{u}_y^1(-1, t) = \boldsymbol{e}_1 \left(G_1(C(\epsilon, t), u_1^0(t)) - G_2(C(-\epsilon, t), u_1^0(t)) \right) = 2(\boldsymbol{u}_t^0 - \boldsymbol{F}(\boldsymbol{u}^0)).$$
(B.6)

Upon rewriting this equation we obtain a system of ODEs for $\boldsymbol{u}^0$ given by

$$\boldsymbol{u}_t^0 = \boldsymbol{F}(\boldsymbol{u}^0) + \frac{\boldsymbol{e}_1}{2} \left[G_1(C(\epsilon, t), u_1^0(t)) - G_2(C(-\epsilon, t), u_1^0(t)) \right].$$
(B.7)

Now letting the width of the cell approach 0, or equivalently $\epsilon \to 0$, we obtain the limiting system

$$\boldsymbol{u}_t^0 = \boldsymbol{F}(\boldsymbol{u}^0) + \frac{\boldsymbol{e}_1}{2} \left[G_1(C(0^+, t), u_1^0(t)) - G_2(C(0^-, t), u_1^0(t)) \right].$$
(B.8)

If we consider the case of linear coupling for which G_1 and G_2 have the forms

$$G_1(C(0^+,t), u_1^0) = \kappa(C(0^+,t) - u_1^0), \qquad G_2(C(0^-,t), u_1^0) = -\kappa(C(0^-,t) - u_1^0), \qquad \text{(B.9)}$$

then (B.8) becomes

$$\boldsymbol{u}_t^0 = \boldsymbol{F}(\boldsymbol{u}^0) + \boldsymbol{e}_1 \left[\frac{\kappa}{2}(C(0^+,t) + C(0^-,t)) - \kappa u_1^0 \right]. \qquad \text{(B.10)}$$

This specifies ODEs for the time evolution of the leading order term for the local species inside the cell, and in this way approximately characterizing the local dynamics. In §4, we drop the superscript in $\boldsymbol{u}^0$ and use (B.10) to describe the local dynamics inside each cell.

C   An Alternative PDE-ODE Formulation for a Periodic Chain

In this appendix we briefly discuss the implications of an alternative formulation of the periodic cell problem (4.1). In this simpler formulation, we assume that $C(x,t)$ is continuous on the ring, but has jumps in the flux DC_x across each cell. This alternative formulation is

$$C_t = DC_{xx} - kC, \quad t > 0, \quad x \in (-L, (2m-1)L), \quad \text{with} \quad x \neq 2jL, \quad j = 0, \ldots, m-1,$$
$$C(-L,t) = C(2mL - L, t), \quad C_x(-L,t) = C_x(2mL - L, t), \qquad \text{(C.1a)}$$
$$[DC_x]\big|_{x=2jL} = 2\kappa \left[C(2jL,t) - u_{1j} \right], \qquad j = 1, \ldots, m,$$

where $[u_x]\big|_{x_0} \equiv u_x(x_0^+) - u_x(x_0^-)$. This bulk field is then coupled to the internal cells dynamics by

$$\frac{d\boldsymbol{u_j}}{dt} = \boldsymbol{F}(\boldsymbol{u_j}) + \boldsymbol{e_1} \left[\kappa C(2jL,t) - \kappa u_{1j} \right], \qquad j = 0, \ldots, m-1. \qquad \text{(C.1b)}$$

For (C.1), we again obtain the symmetric steady-state solution as in §4.1. However, in contrast to the analysis in §4.2, in the linear stability analysis for (C.1) the perturbations in the bulk diffuson field must now be continuous across each cell. From an analysis similar to that in §4.2, we readily derive for the Sel'kov kinetics that the eigenvalue parameter λ satisfies (4.12a), where in place of (4.12b), we have

$$\Delta_\lambda \equiv -\frac{1}{\kappa} + \frac{1}{D\Omega_\lambda} \frac{\sinh(2\Omega_\lambda L)}{\text{Re}(z) - \cosh(2\Omega_\lambda L)}, \qquad \text{Re}(z_l) = \cos\left(\frac{2\pi l}{m}\right), \qquad \text{(C.2)}$$

where Ω_λ is defined in (4.9). As a remark if we set $z_l = 1$ (in-phase) and $z_l = -1$ (anti-phase) in (C.2), we can readily show that (4.12a) with (C.2) reduces, as expected, to the two-cell spectral problem (3.5) of §3.1 for either in-phase or anti-phase modes, respectively, upon setting $\beta = \kappa$ in (3.5).

References

[1] S. M. Baer, T. Erneux, J. Rinzel, *The Slow Passage Through a Hopf bifurcation: Delay, Memory Effects, and Resonance*, SIAM J. Appl. Math., **49**(1), (1989), pp. 5571.

[2] R. Bertram, M. J. Butte, T. Kiemel, A. Sherman, *Topological and Phenomenological Classification of Bursting Oscillations*, Bull. Math. Bio. **57**(3), (1995), pp. 413–439.

[3] W. Y. Chiang, Y. X. Li, P. Y. Lai, *Simple Models for Quorum Sensing: Nonlinear Dynamical Analysis*, Phys. Rev. E., **84**, (2011), 041921.

[4] G. B. Ermentrout, *Simulating, Analyzing, and Animating Dynamical Systems: A Guide to XPPAUT for Researchers and Students*, SIAM 2002, Philadelphia, USA.

[5] A. Goldbeter, *Biochemical Oscillations and Cellular Rhythms: The Molecular Bases of Periodic and Chaotic Behaviour*, Cambridge U. Press, Cambridge, U.K. (1990), 632 pp.

[6] A. Gomez-Marin, J. Garcia-Ojalvo, J. M. Sancho, *Self-Sustained Spatiotemporal Oscillations Induced by Membrane-Bulk Coupling*, Phys. Rev. Lett., **98**(16), (2007), 168303.

[7] J. Gou, Y. X. Li, W. Nagata, *Interactions of In-Phase and Anti-Phase Synchronies in Two Cells Coupled by a Spatially Diffusing Chemical: Double-Hopf Bifurcations*, accepted, I.M.A. J. Applied Math, (2016), (24 pages).

[8] J. Gou, Y. X. Li, W. Nagata, M. J. Ward *Synchronized Oscillatory Dynamics for a 1-D Model of Membrane Kinetics Coupled by Linear Bulk Diffusion*, SIAM J. Appl. Dyn. Sys., **14**(4), (2015), pp. 2096–2137.

[9] J. Gou, M. J. Ward, *Oscillatory Dynamics for a Coupled Membrane-Bulk Diffusion Model with Fitzhugh-Nagumo Membrane Kinetics*, accepted, SIAM J. Appl. Math., (2016), (24 pages).

[10] J. Gou, M. J. Ward, *An Asymptotic Analysis of a 2-D Model of Dynamically Active Compartments Coupled by Bulk Diffusion*, submitted, J. Nonl. Science, (2015), (37 pages).

[11] E. Izhikevich, *Dynamical Systems in Neuorscience: The Geometry of Excitability and Bursting*, MIT Press, Cambridge, MA, USA (2007).

[12] L. Z. Krsmanovic, N. Mores, C. E. Navarro, K. K. Arora, K. J. Catt, *An Agonist-Induced Switch in G Protein Coupling of the Gonadotropin-Releasing Hormone Receptor Regulates Pulsatile Neuropeptide Secretion*, Proc. Natl. Acad. Sci. USA, **100**(5), (2003), pp. 2969–2974.

[13] S. D. Lawley, J. C. Mattingly, M. C. Reed, *Stochastic Switching in Infinite Dimensions with Application to Random Parabolic PDE's*, SIAM J. Math. Analysis, **47**(4), (2015), pp. 3035–3063.

[14] Y. X. Li, A. Khadra, *Robust Synchrony and Rhythmogenesis in Endocrine Neurons via Autocrine Regulations in Vitro and in Vivo*, Bull. Math. Biology, **70**(8), (2008), pp. 2103–2125.

[15] G. Martínez de la Escalera, A. L. H. Choi, R. I. Weiner, *Generation and Synchronization of Gonadotropin-Releasing Hormone (GnRH) Pulses: Intrinsic Properties of the GT1-1 GnRH Neuronal Cell Line* Proc. Natl. Acad. Sci. USA, **89**(5), (1992), pp. 1852–1855.

[16] M. K. McClintock, *Menstrual Synchrony and Suppression*, Nature **229**, (1971), pp. 244–245.

[17] J. Müller, H. Uecker, *Approximating the Dynamics of Communicating Cells in a Diffusive Medium by ODEs - Homogenization with Localization*, J. Math. Biol., **67**(5), (2013), pp. 1023–1065.

[18] J. Müller, C. Kuttler, B. A. Hense, M. Rothballer, A. Hartmann, *Cell-Cell Communication by Quorum Sensing and Dimension-Reduction*, J. Math. Biol., **53**(4), (2006), pp. 672–702.

[19] Y. Nec, M. J. Ward, *An Explicitly Solvable Nonlocal Eigenvalue Problem and the Stability of a Spike for a Sub-Diffusive Reaction-Diffusion System*, Math. Modeling Natur. Phen., **8**(2), (2013), pp. 55–87.

[20] M. J. Russel, G. M. Switz, K. Thompson, *Olfactory Influences on the Human Menstrual Cycle*, Pharm. Biochem. Behav., **13**(5), (1980), pp. 737–738.

[21] E. E. Sel'kov, *Self-Oscillations in Glycolysis*, European J. Biochem., **4**(1), (1968), pp. 79–86.

[22] K. Stern, M. K. McClintock, *Regulation of Ovulation by Human Pheromones*, Nature, **392**, (1998), pp. 177–179.

[23] E. Terasawa, W. K. Schanhofer, K. L. Keen, L. Luchansky, *Intracellular Ca(2+) Oscillations in Luteinizing Hormone-Releasing Hormone Neurons Derived from the Embryonic Olfactory Placode of the Rhesus Monkey*, Jour. of Neuroscience, **19**(14), (1999), pp. 5898–5909.